

# Beyond Output Faithfulness: Learning Attributions that Preserve Computational Pathways

Siyu Zhang  
University of Texas at Austin  
zhangsiyu@utexas.edu

Kenneth Mcmillan  
University of Texas at Austin  
kenmcm@cs.utexas.edu

## Abstract

Faithfulness metrics such as insertion and deletion evaluate how feature removal affects model outputs but overlook whether explanations preserve the computational pathway the network actually uses. We show that external metrics can be maximized through alternative pathways—perturbations that reroute computation via different feature detectors while preserving output behavior. To address this, we propose activation preservation as a tractable proxy for preserving computational pathways.

We introduce *Faithfulness-guided Ensemble Interpretation (FEI)*, which jointly optimizes external faithfulness (via ensemble quantile optimization of insertion/deletion curves) and internal faithfulness (via selective gradient clipping). Across VGG and ResNet on ImageNet and CUB-200-2011, FEI achieves state-of-the-art insertion/deletion scores while maintaining significantly lower activation deviation, showing that both external and internal faithfulness are essential for reliable explanations.

## 1. Introduction

Explainability is a cornerstone of trustworthy AI, and feature attribution methods are among the most widely used tools for interpreting neural network decisions. Evaluation has largely converged on *insertion* and *deletion* metrics [15, 18], which measure how removing features alters model predictions. High scores on these metrics are often treated as definitive evidence of explanation quality.

**We ask: are these metrics sufficient?** Optimization-based methods [7, 8, 25] rely on crude approximations—simplified surrogates and auxiliary regularizers (e.g., sparsity, smoothness) rather than the full metric curve. This raises a fundamental question: *if we could optimize insertion and deletion metrics directly and precisely, would the resulting explanations be meaningful?*

To test this, we introduce *Ensemble Quantile Optimization (EQO)*, a differentiable formulation that directly mod-

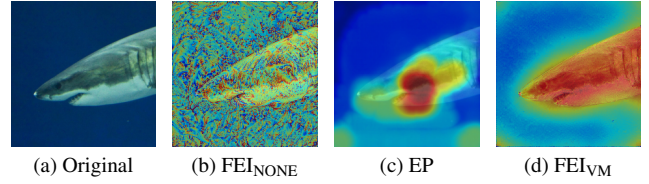


Figure 1. **External metrics alone are insufficient.** (b)  $\text{FEI}_{\text{NONE}}$ : direct optimization of insertion/deletion without constraints produces noisy artifacts despite the highest metric scores. (c) EP [7]: approximate optimization with smoothness regularization. (d)  $\text{FEI}_{\text{VM}}$ : precise optimization with internal pathway constraints yields coherent attributions while maintaining competitive external scores.

els the complete insertion/deletion curve across perturbation levels. Unlike prior surrogates, EQO provides exact gradient flow without convergence ambiguity, enabling a direct evaluation of the metrics themselves.

This diagnostic experiment reveals a critical gap: optimizing external metrics alone (our baseline,  $\text{FEI}_{\text{NONE}}$ ) permits spurious solutions. Despite achieving the highest insertion scores (Tab. 1),  $\text{FEI}_{\text{NONE}}$  produces visually noisy artifacts (Fig. 1), generates spurious explanations on blank images (Sec. 4.2), and disrupts internal activation patterns by  $6\times$  compared to constrained variants (Tab. 3).

This exposes a fundamental flaw: insertion/deletion metrics capture *whether* features influence predictions but not *how* they do so. High external scores can arise from explanations that exploit shortcut pathways inconsistent with the model’s internal reasoning. We therefore argue that explanation quality requires two complementary dimensions:

- **External faithfulness:** Removing attributed features should meaningfully alter the output.
- **Internal faithfulness:** Perturbations should preserve the network’s computational pathway.

We use “computational pathway” to refer informally to which network components actually matter for a prediction: the feature detectors, intermediate representations, and processing mechanisms that transform input to output.

Motivated by mechanistic interpretability [3, 5, 6, 14] and adversarial robustness [10, 28], we use *activation preservation* as a practical proxy for internal faithfulness: preserving layer-wise activations maintains the model’s computational pathway, while large deviations indicate pathway changes.

**Our Approach.** We propose *Faithfulness-guided Ensemble Interpretation (FEI)*, which enforces both external and internal faithfulness through two complementary mechanisms: (1) *Ensemble Quantile Optimization* for differentiable modeling of insertion/deletion curves, and (2) *Selective gradient clipping* to prevent activation-disrupting updates without sacrificing optimization flexibility. This combination eliminates spurious solutions while achieving state-of-the-art external performance.

#### Contributions.

- **Conceptual:** Establish that external and internal faithfulness are not aligned yet complementary—both are important for reliable explanations.
- **Technical:** Introduce Ensemble Quantile Optimization for precise metric optimization and selective gradient clipping for pathway preservation.
- **Empirical:** Across ImageNet and CUB-200-2011 with VGG and ResNet, constrained FEI variants achieve competitive or superior External Faithfulness while maintaining strong Internal Faithfulness.

## 2. Related Work

### 2.1. Attribution Methods

Feature attribution methods explain model predictions by assigning importance scores to input features.

**Backpropagation-based methods** propagate relevance from outputs to inputs. Early work used raw gradients for saliency maps [21], with later improvements enhancing sharpness and stability via gradient smoothing [22], guided backpropagation [23], and Integrated Gradients [24]. Extensions integrate intermediate layers [2] or alternative integration paths [12]. While efficient, these methods often highlight low-level edges and textures.

**Activation-based methods** visualize discriminative internal activations. CAM [31] and Grad-CAM [19] localize class-relevant regions in the final convolutional layer. Variants improve precision via DeepLIFT-based lifting (Lift-CAM [11]), channel weighting (Score-CAM [27]), or relevance propagation (FG-CAM [16]). These produce interpretable maps but remain limited by the spatial granularity of final-layer features.

**Perturbation-based methods** assess importance by measuring output changes under input modifications. Occlusion tests mask image patches, RISE [15] estimates importance stochastically, and Shapley-value-based formulations provide counterfactual explanations [13, 30].

**Faithfulness optimization methods** directly optimize attribution maps to maximize faithfulness metrics [7, 8, 25]. However, prior approaches rely on surrogate objectives (e.g., single perturbation steps, smoothness regularizers), leaving unaddressed the risk of exploiting spurious solutions from *approximate* external faithfulness—a gap we investigate. Our method, *Faithfulness-guided Ensemble Interpretation (FEI)*, builds on this line by introducing *ensemble quantile optimization* for *precise* external metric modeling and *selective gradient clipping* to simultaneously enforce internal faithfulness.

### 2.2. Faithfulness and Mechanistic Analysis

**Faithfulness metrics.** Attribution evaluation typically relies on insertion and deletion tests [18], which measure output changes as features are progressively added or removed. As we establish in our introduction, these metrics capture what we term *external faithfulness*—alignment between feature importance and output behavior—but are insufficient on their own.

**Mechanistic Interpretability (MI).** Contemporary work [3, 14, 29] investigates how models compute internally, showing that hidden activations function as hierarchical feature detectors. Concepts like superposition [6] and sparse autoencoders (SAEs) [5] further explain how features are represented. These findings provide the theoretical grounding for our proposal: that explanations should also be evaluated on their ability to preserve the model’s internal computational pathway, motivating our use of *activation preservation* as a proxy for *internal faithfulness*.

## 3. Method

We aim to generate explanations that are both *externally faithful*—reflecting the causal effect of input features on predictions—and *internally consistent*—maintaining the model’s computational pathway. In this section, We formalize this goal, introduce a differentiable metric optimization, add an activation preservation constraint, and unify these components in our FEI framework (Algorithm 1)

### 3.1. Attribution Map

Given an input image  $x \in \mathbb{R}^{H \times W \times C}$  and a model  $f$ , let  $\psi_f(x, y_t)$  denote the predicted probability for a target class  $y_t$ . An attribution map  $M \in \mathbb{R}^{H \times W}$  assigns an importance score  $M[p]$  to each spatial position  $p$ , quantifying the contribution of the feature  $x[p]$  to  $y_t$ .

### 3.2. External Faithfulness

Insertion and deletion metrics evaluate how model confidence changes as important pixels are progressively added or removed [15]. To simplify notation, let  $\phi(\tilde{x}) = \psi_f(\tilde{x}, y_t)$  represent the predicted probability of the target class  $y_t$  for an input image  $\tilde{x}$ . Let  $R$  be a reference image. Given an

attribution map  $M$ , define  $u_q(M)$  and  $l_q(M)$  as the top and bottom  $q$ -fraction of pixels, respectively. The metrics are:

$$V_{\text{Ins}}(\phi, M, x) = \frac{1}{k} \sum_{q \in \mathcal{Q}} \phi(x \otimes l_q(M)), \quad (1)$$

$$V_{\text{Del}}(\phi, M, x) = \frac{1}{k} \sum_{q \in \mathcal{Q}} \phi(x \otimes u_q(M)), \quad (2)$$

where  $\mathcal{Q} = \{q_1, \dots, q_k\}$  and  $x \otimes S$  replaces pixel set  $S$  in  $x$  with  $R$ . Higher  $V_{\text{Ins}}$  and lower  $V_{\text{Del}}$  indicate stronger external faithfulness. However, these metrics evaluate input-output consistency only; they do not ensure that the same internal computation underlies the observed effect.

### 3.3. Differentiable Proxy

Directly optimizing insertion or deletion curves is intractable because binary masks and discrete quantiles are non-differentiable. Prior works [7, 8] approximate them with single perturbation step, which yields noisy gradients, poor convergence, and ambiguous results: it remains unclear whether suboptimal performance arises from limited approximation or from the inadequacy of the underlying metrics themselves.

We propose a differentiable *ensemble quantile optimization* (EQO) framework that models the full sequence of quantile perturbations continuously. Unlike previous methods, EQO provides a differentiable approximation of the entire metric curve. For brevity, we present the approximation for the insertion metric; the deletion objective can be defined analogously.

Let  $\mathcal{P}$  denote the set of all pixels in the image. For each quantile level  $q \in \mathcal{Q}$ , we define a continuous retention map  $\alpha_q \in [0, 1]^{|\mathcal{P}|}$  approximating the retention set (i.e., the complement of  $l_q(M)$ ), where  $\alpha_q[p]$  denotes the probability that pixel  $p$  is retained. The constraint

$$\sum_{p \in \mathcal{P}} \alpha_q[p] = (1 - q)|\mathcal{P}| \quad (3)$$

preserves the fraction of unmasked pixels. The expected perturbed image is

$$\tilde{x}(\alpha_q) = \alpha_q \odot x + (1 - \alpha_q) \odot R. \quad (4)$$

The insertion loss is

$$\mathcal{L}_{\text{ins}}(\alpha_q) = -\phi(\tilde{x}(\alpha_q)) + \beta \left| \sum_{p \in \mathcal{P}} \alpha_q[p] - (1 - q)|\mathcal{P}| \right|, \quad (5)$$

where  $\beta > 0$  enforces the quantile constraint.

To ensure monotonic consistency ( $l_{q_i} \subseteq l_{q_{i+1}}$ ), we parameterize  $\{\alpha_{q_i}\}_{i=1}^k$  using non-negative increments  $\delta_{q_i} = \alpha_{q_i} - \alpha_{q_{i+1}}$ , with  $\alpha_{q_{k+1}} = \mathbf{0}$ . During optimization, we project  $\alpha_{q_i}$  to  $[0, 1]$ . The final attribution is aggregated as:

$$M = \frac{1}{k} \sum_{i=1}^k \alpha_{q_i}. \quad (6)$$

---

#### Algorithm 1: Faithfulness-guided Ensemble Interpretation (FEI)

---

**Input:** image  $x$ , ref  $R$ , func  $\phi$ , quantiles  $\mathcal{Q}$ , iters  $T$ , step  $\eta$ ,  $\beta$ , variant

**Output:** attribution map  $M$

initialize  $\{\alpha_{q_i}\}$  as 0;

$\{h^\ell\}_{\ell=1}^L \leftarrow \text{ForwardPass}(\phi(x))$ ;

**for**  $q_i \in \mathcal{Q}$  **do**

**for**  $t = 1$  **to**  $T$  **do**

$\tilde{x} \leftarrow \alpha_{q_i} \odot x + (1 - \alpha_{q_i}) \odot R$ ;

$\mathcal{L}_{\text{con}} \leftarrow \beta \cdot \left| \sum_p \alpha_{q_i}[p] - (1 - q_i)|\mathcal{P}| \right|$ ;

$\mathcal{L}_{\text{ins}} \leftarrow -\phi(\tilde{x}) + \mathcal{L}_{\text{con}}$ ;

        compute  $\gamma_h^\ell = \partial \mathcal{L}_{\text{ins}} / \partial \tilde{h}^\ell$  for all conv layers;

$\tilde{\gamma}_h^\ell \leftarrow \text{ClipGrad}(\gamma_h^\ell, h^\ell, \tilde{h}^\ell, \text{variant})$ ;

        backpropagate  $\{\tilde{\gamma}_h^\ell\}$  to obtain  $g_\alpha$ ;

$\alpha_{q_i} \leftarrow \alpha_{q_i} - \eta g_\alpha$ ;

**return**  $M = \sum_i \alpha_{q_i}$

---

**Intuition.** EQO provides smooth gradient flow over the entire insertion curve, aligning the optimization objective with the evaluation metric. Compared to stochastic perturbation or single-step methods, EQO captures richer gradient information, stabilizes optimization, and exposes cases where different internal pathways yield equivalent external scores—motivating the internal constraint introduced next.

### 3.4. Internal Faithfulness

**Motivation.** Optimizing only external faithfulness produces pathological behaviors. FEI<sub>None</sub> achieves the highest insertion scores (Tab. 1) yet shows (1)  $2\times$  lower activation cosine similarity and  $6\times$  higher activation deviation (Tab. 3), (2) 92–98% spurious blank-image attributions compared to 0–0.4% for constrained variants (Sec. 4.2), and (3) visually noisy artifacts (Fig. 3). This indicates that external metrics can be maximized by rerouting computation through alternative activation circuits that yield equivalent outputs. Thus, an explanation may appear faithful in outcome while being mechanistically inconsistent with the model’s actual reasoning.

**A Practical Proxy: Activation Preservation.** We therefore constrain perturbations to preserve the model’s activation dynamics. While other internal metrics may also capture pathway changes, we focus on layer-wise activation similarity for its computational efficiency and direct interpretability. We hypothesize that significant deviation in this internal state indicates engagement of different computational mechanisms. For a deterministic network,

$$h_{\ell+1} = f_\ell(h_\ell; W_\ell), \quad (7)$$

where  $h_\ell \in \mathbb{R}^{d_\ell}$  denotes post-ReLU activations. We en-

force this proxy by encouraging  $\tilde{h}_\ell \approx h_\ell$  across layers, where  $\tilde{h}_\ell$  is the activation under the perturbed input.

**Justification.** We justify it with complementary reasoning:

*Forward (sufficiency):* If activations remain consistent across layers, each transformation  $f_\ell$  receives effectively the same inputs, preserving the causal composition of the network’s computation.

*Backward (plausibility):* Mechanistic interpretability studies show that features are represented as directions in sparse, overlapping subspaces [5, 6, 14]. Under the superposition hypothesis, as features are not orthogonal, the network must actively suppress irrelevant feature direction to maintain functional coherence. Large deviations in later-layer activations are therefore more likely to correspond to changes in which task-relevant features are active, suggesting engagement of different computational mechanisms. Evidence from adversarial robustness supports this view: small activation perturbations can cause semantic output shifts [10, 28]. The low cosine similarity and high deviation for  $\text{FEI}_{\text{None}}$  aligns with such pathway alteration rather than benign noise.

**Empirical validation.** To assess whether activation preservation serves as a useful proxy, we examine three independent behaviors: methods with stronger preservation should (1) avoid spurious attributions (Sec. 4.2), (2) maintain competitive external faithfulness (Tab. 1), and (3) produce coherent visualizations (Fig. 3). Our results demonstrate all three properties, indicating that activation preservation effectively distinguishes optimization behaviors that maintain model-consistent computations from those that exploit alternative circuits to achieve high external scores.

**Evaluation metrics.** We measure preservation using: (1) **Cosine Similarity**—capturing structural similarity; and (2) **Mean Squared Error (MSE)**—capturing magnitude deviation; high similarity and Low MSE jointly indicate strong internal faithfulness.

### 3.5. Selective Gradient Clipping

Directly penalizing activation deviations (e.g., via an  $L_2$  loss) requires careful layer-wise hyperparameter balancing and is prone to instability in deep networks. We instead enforce preservation implicitly using *selective gradient clipping* (ClipGrad). This method is derived in Sec. D from a principled objective, resulting in a universal clipping rule. ClipGrad provides local, non-parametric control: it prevents updates that would disrupt the original activation pattern while leaving compatible gradients untouched.

Let  $\gamma_h = \partial \mathcal{L}_{\text{ins}} / \partial \tilde{h}^\ell$  denote the gradient with respect to layer- $\ell$  activations, where  $i$  indexes individual neurons. We redefine  $\gamma_h$  based on layer-wise activation states. The ClipGrad operation (see Algorithm 1) applies one of four constraint variants, each encoding a different strategy:

**Value Matching (VM):** Strictly enforces  $\tilde{h}^\ell = h^\ell$  by blocking any increase or decrease in activations:

$$\tilde{\gamma}_h[i] = \begin{cases} 0 & \text{if } (\gamma_h[i] \leq 0 \wedge \tilde{h}^\ell[i] > h^\ell[i]) \\ & \vee (\gamma_h[i] > 0 \wedge \tilde{h}^\ell[i] \leq h^\ell[i]) \\ \gamma_h[i] & \text{otherwise.} \end{cases} \quad (8)$$

**Inactivated Value Matching (IVM):** Prevents spurious activation by disallowing increases beyond the original value:

$$\tilde{\gamma}_h[i] = \begin{cases} 0 & \text{if } \gamma_h[i] \leq 0 \wedge \tilde{h}^\ell[i] > h^\ell[i] \\ \gamma_h[i] & \text{otherwise.} \end{cases} \quad (9)$$

**Activated Value Matching (AVM):** Prevents suppression of originally active neurons:

$$\tilde{\gamma}_h[i] = \begin{cases} 0 & \text{if } \gamma_h[i] > 0 \wedge \tilde{h}^\ell[i] \leq h^\ell[i] \\ \gamma_h[i] & \text{otherwise.} \end{cases} \quad (10)$$

**Inactivated Binary Matching (IBM):** Blocks activation of originally inactive neurons:

$$\tilde{\gamma}_h[i] = \begin{cases} 0 & \text{if } \gamma_h[i] \leq 0 \wedge h^\ell[i] \leq 0 \\ \gamma_h[i] & \text{otherwise.} \end{cases} \quad (11)$$

These variants provide a principled trade-off between constraint strength and flexibility. VM enforces strict equality of internal states, while IBM allows maximum expressivity. IVM and AVM represent asymmetric intermediate cases. All variants require no architecture-specific hyperparameters or implementation changes

**Complete Framework.** Algorithm 1 summarizes the full **Faithfulness-guided Ensemble Interpretation (FEI)** procedure, which integrates the differentiable external optimization of EQO (Sec. 3.3) with the internal constraints of ClipGrad (Sec. 3.5). Together, they yield explanations that are both externally faithful—preserving model predictions—and internally faithful—maintaining consistent activation pathways throughout the network.

## 4. Experiments

We evaluate our approach on multiple CNN architectures and datasets to assess both *external* and *internal faithfulness*. Our goal is to understand whether the proposed FEI framework not only aligns with model predictions but also preserves the internal computational process responsible for those predictions.

We organize our evaluation to answer three key questions that follow our diagnostic narrative: (1) Do high scores on external metrics guarantee a good explanation, or do they decouple from basic robustness checks? (2) Is such decoupling linked to a measurable breakdown in the model’s



Table 1. Quantitative Faithfulness Evaluation Across Two Datasets and Two Models

	CUB-200-2011				ImageNet			
	VGG16		ResNet50		VGG16		ResNet50	
	Ins.↑	Del.↓	Ins.↑	Del.↓	Ins.↑	Del.↓	Ins.↑	Del.↓
FG-VCE [30]	0.738±0.045	0.094±0.019	0.615±0.044	0.106±0.018	0.487±0.051	0.114±0.023	0.566±0.038	0.149±0.027
GradCAM [19]	0.728±0.045	0.079±0.015	0.612±0.044	0.098±0.016	0.453±0.050	0.102±0.019	0.563±0.042	0.139±0.023
Extremal Perturbation [7]	0.727±0.044	0.095±0.019	0.595±0.049	0.098±0.019	0.473±0.052	0.130±0.022	0.516±0.045	0.149±0.025
Lift-CAM [11]	0.724±0.044	0.077±0.014	0.610±0.045	0.097±0.016	0.483±0.050	0.097±0.019	0.554±0.043	0.141±0.023
GradCAM++ [4]	0.718±0.043	0.093±0.016	0.610±0.045	0.096±0.016	0.477±0.050	0.119±0.021	0.553±0.043	0.142±0.023
ScoreCAM [27]	0.716±0.045	0.082±0.014	0.611±0.046	0.094±0.015	0.486±0.049	0.101±0.018	0.554±0.042	0.145±0.023
IIA [2]	0.709±0.046	0.091±0.017	0.607±0.045	0.098±0.016	0.437±0.050	0.109±0.020	0.549±0.042	0.134±0.023
RISE [15]	0.697±0.050	0.082±0.017	0.583±0.050	0.085±0.017	0.431±0.050	0.103±0.017	0.480±0.047	0.125±0.018
Saliency [21]	0.498±0.025	0.043±0.005	0.339±0.022	0.082±0.010	0.210±0.015	0.076±0.010	0.257±0.017	0.125±0.013
Smoothgrad [22]	0.638±0.025	0.047±0.005	0.514±0.027	0.060±0.006	0.339±0.019	0.075±0.009	0.395±0.021	0.117±0.013
Integrated Gradient [24]	0.097±0.030	<b>0.033±0.009</b>	0.118±0.026	0.050±0.012	0.098±0.025	<b>0.039±0.010</b>	0.154±0.032	<b>0.065±0.015</b>
FEI <sub>IBM</sub>	<b>0.753±0.023</b>	0.051±0.005	<b>0.647±0.026</b>	<b>0.044±0.004</b>	<b>0.566±0.024</b>	0.081±0.009	<b>0.626±0.022</b>	0.093±0.010
FEI <sub>AVM</sub>	0.732±0.026	0.055±0.005	0.636±0.026	0.054±0.005	0.557±0.022	0.080±0.010	0.601±0.024	0.113±0.011
FEI <sub>VM</sub>	0.724±0.025	0.072±0.007	0.634±0.027	0.054±0.005	0.512±0.025	0.117±0.011	0.590±0.023	0.121±0.013
FEI <sub>IVM</sub>	0.713±0.023	0.079±0.007	0.615±0.027	0.059±0.005	0.489±0.025	0.130±0.013	0.561±0.024	0.135±0.014
FEI <sub>NONE</sub>	0.778±0.026	0.095±0.013	0.772±0.018	0.112±0.012	0.729±0.015	0.185±0.017	0.849±0.014	0.207±0.018

internal pathway? (3) Can we fix this internal breakdown while boosting state-of-the-art external performance?

To answer these questions, we run diagnostic tests( Sec. 4.2), layer-wise activation analyses( Sec. 4.3), standard insertion/deletion evaluations( Sec. 4.4), and qualitative visual comparisons( Sec. 4.5).

#### 4.1. Experimental Setup

**Datasets and Models.** **Datasets and Models.** We experiment on CUB-200-2011 [26] (fine-grained) and ImageNet [17] (large-scale) using VGG16 [20] and ResNet50 [9], two canonical CNNs that differ in depth and connectivity. We sample 1,000 images per dataset and report averages over 3 runs with standard deviation.

**Implementation Details.** FEI variants are optimized using Adam for 100 iterations per quantile. We use randomly sampled mono-chromatic images as the reference  $R$  and optimize over quantiles  $\{0.1, 0.3, 0.5, 0.7, 0.9\}$  with  $\beta = 0.1$ . ClipGrad is applied to all convolutional layers.

**Ablation Studies.** Detailed ablations (Sec. A) validate our core methodology and design choices: (1) EQO demonstrates clear supremacy over L1 area regularization across all metrics; without any area constraint, optimization fails completely. (2) We validate our choice to clip all layers by identifying a cascade effect: constraining only early layers (1–16) achieves significantly better internal preservation than constraining only later layers. This shows that early-layer deviations compound and that preventing pathway divergence requires constraining the network from its earliest layers. (3) Performance saturates around 100 iterations, confirming efficiency. (4) Our method is robust to quantile granularity (3, 5, or 9 levels perform similarly), and  $\beta = 0.1$  is sufficient to enforce the constraint.

Table 2. **Diagnostic test: black image defense.** Fraction of black images producing attributions. Lower is better. \*FGVis uses color-space optimization; not directly comparable.

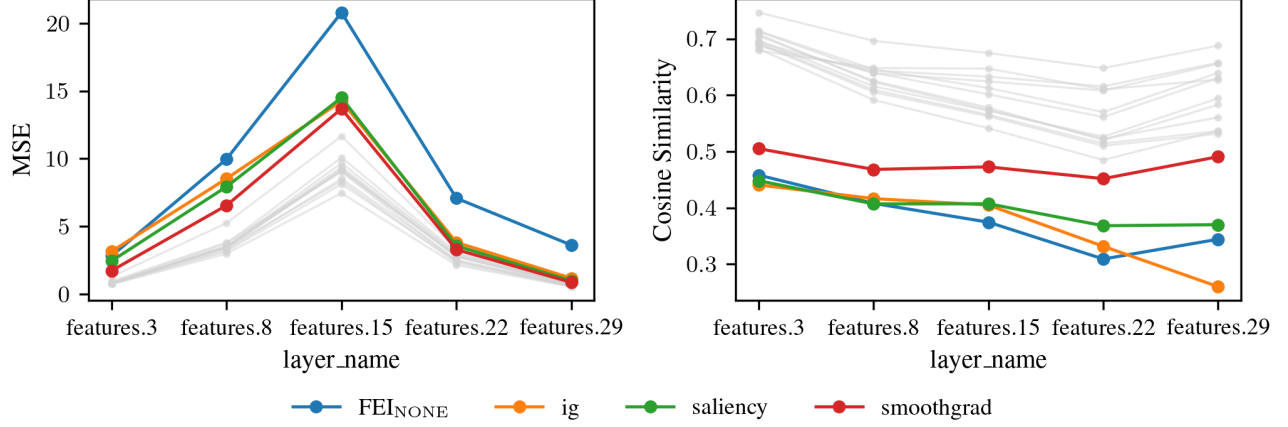
Model	FGVis*	FEI <sub>IBM</sub>	FEI <sub>IVM</sub>	FEI <sub>AVM</sub>	FEI <sub>VM</sub>	FEI <sub>None</sub>
AlexNet	0.1%	0.4%	0.2%	93.8%	0.1%	92.8%
ResNet50	0.1%	0.1%	0%	0.1%	0.1%	97.1%
VGG16	0.1%	0.1%	0.1%	95.2%	0.1%	94.7%
GoogLeNet	0.1%	0%	0.2%	0%	0%	97.9%

#### 4.2. Diagnostic Test: Black Image Defense

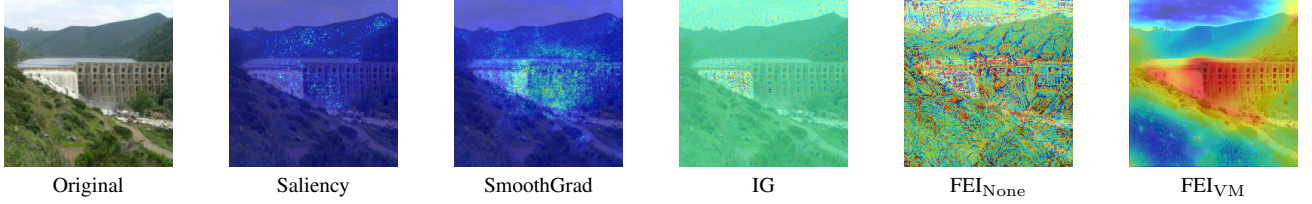
We first test our central hypothesis: that external metrics alone are insufficient and can be exploited. We use a “black image defense” test [25] where methods are given a meaningless (all-black) input. A robust method should produce no explanation; a non-trivial attribution indicates the method is exploiting spurious pathways.

**Evaluation setup.** The original framework [25] uses a single-step crude approximation with L1 regularization. To isolate approximation artifacts from approach limitations, we implement FGVis within our EQO framework, enabling a fair comparison under equivalent optimization quality. However, we emphasize that FGVis results are not included in main quantitative comparisons ( Tab. 1–Tab. 3) as it operates in a fundamentally different space—optimizing continuous color channels rather than pixel masking.

**Results.** Table 2 confirms our hypothesis. Our unconstrained optimizer, FEI<sub>None</sub>, generates spurious attributions for 92–98% of black images across all architectures. This demonstrates that an optimizer tasked only with maximizing external faithfulness will freely activate spurious pathways to achieve its goal.



(a) Quantitative layer-wise metrics: fine-grained methods act as outliers (lower MSE, higher Similarity are better). Additional details in Sec. C



(b) Qualitative maps show that internal constraints (e.g., FEI<sub>VM</sub>) preserve coherent, object-focused features compared to gradient-based methods.

Figure 2. Internal faithfulness analysis. Quantitative metrics (left) and qualitative visualizations (right) jointly demonstrate that FEI preserves both internal structure and meaningful spatial patterns.

In sharp contrast, our constrained variants (FEI<sub>IBM</sub>, FEI<sub>IVM</sub>, and FEI<sub>VM</sub>) achieve near-zero failure rates (0–0.4%). This shows that enforcing internal constraints is essential for robust explanations.

**Analysis of Failure Mode.** The contrast between AVM and IVM isolates the causal mechanism. FEI<sub>AVM</sub> fails catastrophically on sequential architectures like AlexNet and VGG16 (93.8% and 95.2%), while FEI<sub>IVM</sub> succeeds (0–0.2%). Critically, on multi-branch architectures (ResNet50, GoogLeNet), FEI<sub>AVM</sub> also achieves near-zero rates. This confirms that blocking activation increases is essential for sequential networks, but not for multi-branch networks where skip connections provide stabilization. More analysis on architectural interaction can be found in Sec. B.

### 4.3. Internal Faithfulness Analysis

Our diagnostic test shows that unconstrained optimization fails; we now investigate *why*. We quantify activation preservation using cosine similarity and MSE, which assess deviation from the model’s original computational pathway. This section addresses our second guiding question: Is the decoupling linked to a measurable internal breakdown?

**Key finding: External and internal objectives are not aligned.** The core of our paper’s thesis is demonstrated by comparing Table 1 and Table 3: FEI<sub>NONE</sub> attains the highest insertion scores yet the worst activation preserva-

tion. This confirms that the diagnostic failure (Q1) is indeed linked to a catastrophic internal breakdown (Q2). A method can appear externally faithful while completely altering the model’s internal computation.

**Unconstrained failure mechanism.** As shown in Table 3, the unconstrained FEI<sub>NONE</sub> results in this internal disruption. This breakdown is the underlying cause for the symptoms we observed: (1) spurious blank-image attributions (Tab. 2), (2) severe cosine similarity degradation (Tab. 3), and (3) noisy visual artifacts (Fig. 3).

**Mitigation via selective clipping.** Enforcing activation constraints eliminates these failures. Our constrained methods achieve dramatically better internal faithfulness; for example, FEI<sub>VM</sub> achieves 6.6× lower MSE and 2× higher cosine similarity on VGG16 than FEI<sub>NONE</sub> (answering the “fix” part of Q3).

**Layer-wise analysis.** Figure 2a shows this failure is consistent across layers. Gradient-based methods and FEI<sub>NONE</sub> exhibit substantially larger deviations, producing noisy, fragmented attributions (Fig. 2b). Activation-based methods (e.g., GradCAM++, ScoreCAM) achieve moderate preservation, with GradCAM++ being the best among non-FEI baselines. Critically, While gradient methods already perform poorly on both structural similarity (Cosine) and activation magnitude (MSE), FEI<sub>NONE</sub>’s failure is even more severe, exhibiting a catastrophically worse MSE.

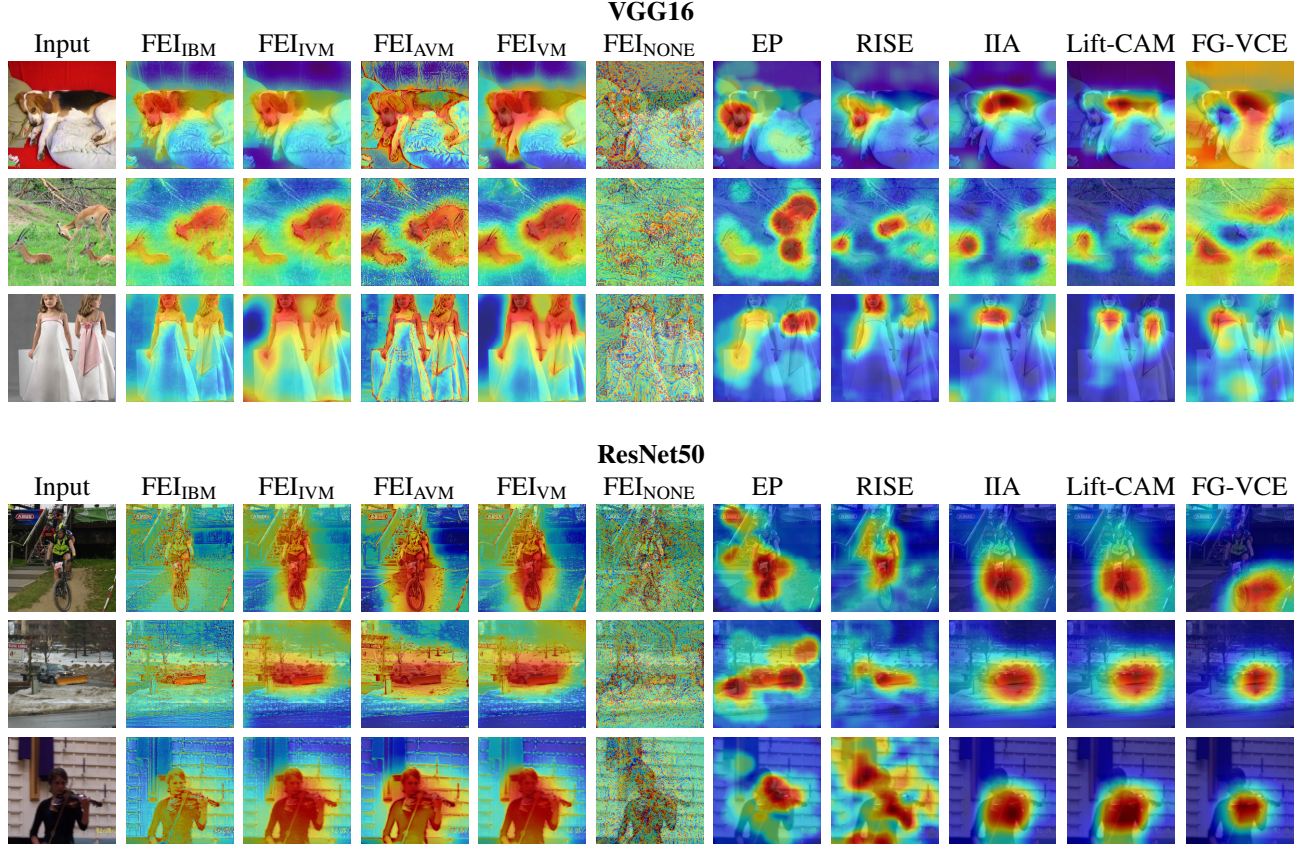


Figure 3. **Visual comparison of attribution methods.** Columns show FEI variants, Extremal Perturbation (EP), RISE, IIA, Lift-CAM, and FG-VCE. Constrained FEI variants yield more focused, object-aligned explanations compared to baselines, which often highlight background or diffuse regions.

#### 4.4. Quantitative External Faithfulness

Having established that our constrained FEI variants solve the pathological failures and internal disruptions (Sec. 4.2 and Sec. 4.3), we now answer our final guiding question: can they do so without sacrificing external performance? As shown in Tab. 1, the answer is yes.

**Constrained FEI vs. Baselines.** Our constrained variants achieve state-of-the-art external scores, proving that internal faithfulness does not require an external trade-off.

**Insertion Performance.**  $\text{FEI}_{\text{IBM}}$  consistently ranks first or second across all configurations, demonstrating exceptional robustness. While FG-VCE is comparable on VGG16/CUB, it performs much worse on ImageNet, highlighting  $\text{FEI}_{\text{IBM}}$ 's superior generalization.

**Deletion Performance.**  $\text{FEI}_{\text{IBM}}$  also achieves competitive deletion scores, maintaining a top rank among non-gradient methods. This is a crucial finding: unlike gradient-based methods, which exhibit a catastrophic trade-off (i.e., poor insertion performance), our method achieves strong performance on both metrics.

**FEI Variant Comparison.** Among the constrained vari-

ants,  $\text{FEI}_{\text{IBM}}$  achieves the best overall external performance. Its asymmetric design—preventing only inactive neurons from activating—appears to provide the ideal balance between optimization flexibility and internal constraint.

#### 4.5. Qualitative Comparison

Figure 3 visualizes attribution maps on ImageNet samples across VGG16 and ResNet50. Warm regions (red) indicate higher importance for the model's decision, while cool regions (blue) denote less relevant areas. This visual analysis confirms our quantitative findings. First, the unconstrained  $\text{FEI}_{\text{NONE}}$  consistently produces noisy, incoherent, and fragmented attributions. This visually demonstrates the pathological behavior identified in our diagnostic (Sec. 4.2) and internal (Sec. 4.3) analyses.

In contrast, Our constrained FEI variants yield fine-grained, spatially coherent, and semantically aligned attributions that capture object contours without artifacts. Among the external baselines, Lift-CAM produces the most competitive maps, yet its heatmaps remain more diffuse than ours—particularly in deeper model such as ResNet50.



Table 3. Internal activation Matching across attribution methods on last feature extraction layer. Lower MSE and higher cosine similarity indicate better internal faithfulness.

Method	MSE ↓		Cosine Similarity ↑	
	VGG16	ResNet50	VGG16	ResNet50
GradCAM++	0.573	0.495	0.640	0.708
ScoreCAM	0.588	0.491	0.631	0.709
Lift-CAM	0.648	0.500	0.594	0.704
GradCAM	0.755	0.505	0.537	0.701
FG-VCE	0.742	0.540	0.536	0.677
IIA	0.765	0.514	0.531	0.694
RISE	0.731	0.588	0.561	0.654
Extremal Perturbation	0.671	0.577	0.583	0.661
SmoothGrad	0.862	0.629	0.491	0.627
Saliency	0.984	0.736	0.370	0.546
Integrated Gradients	1.173	0.817	0.260	0.485
FEI <sub>VM</sub>	<b>0.545</b>	<u>0.412</u>	<b>0.688</b>	<u>0.758</u>
FEI <sub>IVM</sub>	<u>0.567</u>	0.435	0.656	0.743
FEI <sub>IBM</sub>	0.629	0.415	<u>0.658</u>	0.757
FEI <sub>AVM</sub>	0.952	<b>0.399</b>	0.628	<b>0.766</b>
FEI <sub>NONE</sub>	3.619	1.494	0.344	0.592

Among our variants, FEI<sub>VM</sub> provides the most balanced visualizations, combining accurate object localization with detailed structure. FEI<sub>IBM</sub> tends to produce slightly more diffuse activations on ResNet50 while maintaining object focus. FEI<sub>IVM</sub> occasionally attributes relevance to background context. FEI<sub>AVM</sub> may introduce edge-like artifacts on VGG16, linking to the architectural sensitivity seen in our diagnostic test.

Overall, Our constrained FEI variants achieve more precise and faithful attributions than baseline methods, accurately highlighting relevant image regions. Fine-grained visual coherence emerges as a natural byproduct of activation preservation rather than through explicit smoothness constraints.

#### 4.6. Sanity Check

Following Adebayo *et al.* [1], we examine whether attributions appropriately depend on learned model parameters through cascading randomization (Fig. 4). Layers are progressively randomized from top to bottom; explanations should gradually lose structure and object focus as the model loses semantic information. We present the result of FEI<sub>IBM</sub> as it is the least constrained version of our method.

Figure 4 shows the expected behavior for FEI: as more layers are randomized, explanations progressively lose object focus and degrade into noise, confirming appropriate parameter sensitivity. Note that low-level edge patterns per-

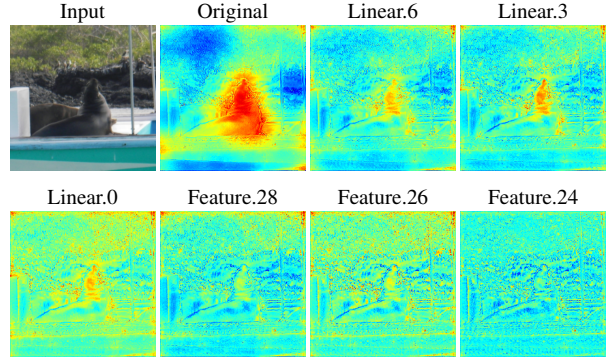


Figure 4. **Sanity check via cascading randomization.** As layers are progressively randomized (left to right, top to bottom), attributions gradually lose object focus, indicating appropriate parameter sensitivity. Example: *Sea Lion* with VGG16 and FEI<sub>IBM</sub>.

sist longer than high-level object structure—this is expected because activation preservation ensures that early layers retain learned low-level features until randomized, and our activation preservation constraints maintain consistency with these unrandomized layers. This behavior confirms proper parameter sensitivity.

The gradual degradation from semantic structure to noise confirms that FEI depends on learned parameters rather than exploiting input artifacts or edge priors.

## 5. Conclusion and Limitations

We demonstrated that standard external faithfulness metrics, such as insertion and deletion, are insufficient for guaranteeing explanation quality. Optimizing them alone leads to pathological solutions by failing to preserve the model’s *internal faithfulness*—its computational pathway. To solve this, we proposed Faithfulness-guided Ensemble Interpretation (FEI), which jointly optimizes external faithfulness (via Ensemble Quantile Optimization) and internal faithfulness (via selective gradient clipping). Our experiments show FEI eliminates these pathological failures while attaining state-of-the-art external faithfulness, confirming that reliable explanations must be both externally predictive and internally consistent.

**Limitations and Future Work.** Our current implementation focuses on CNNs with ReLU-like activations. While the principle of dual faithfulness generalizes, extending it to other architectures, such as Vision Transformers, is a key step; for ViTs, attention pattern alignment may serve as a natural analogue to pathway preservation. Furthermore, our work relies on activation preservation as a *proxy* for pathway consistency. Future work should explore alternative internal metrics (e.g., semantic detector activation) and formally analyze their trade-offs.



## References

- [1] Julius Adebayo, Justin Gilmer, Michael Muelly, Ian Goodfellow, Moritz Hardt, and Been Kim. Sanity checks for saliency maps. *Advances in neural information processing systems*, 31, 2018. 8
- [2] Oren Barkan, Yuval Asher, Amit Eshel, Noam Koenigstein, et al. Visual explanations via iterated integrated attributions. In *Proceedings of the IEEE/CVF International Conference on Computer Vision*, pages 2073–2084, 2023. 2, 5
- [3] David Bau, Bolei Zhou, Aditya Khosla, Aude Oliva, and Antonio Torralba. Network dissection: Quantifying interpretability of deep visual representations. In *Proceedings of the IEEE conference on computer vision and pattern recognition*, pages 6541–6549, 2017. 2
- [4] Aditya Chattopadhyay, Anirban Sarkar, Prantik Howlader, and Vineeth N Balasubramanian. Grad-cam++: Generalized gradient-based visual explanations for deep convolutional networks. In *2018 IEEE winter conference on applications of computer vision (WACV)*, pages 839–847. IEEE, 2018. 5
- [5] Hoagy Cunningham, Aidan Ewart, Logan Riggs, Robert Huben, and Lee Sharkey. Sparse autoencoders find highly interpretable features in language models. *arXiv preprint arXiv:2309.08600*, 2023. 2, 4
- [6] Nelson Elhage, Tristan Hume, Catherine Olsson, Nicholas Schiefer, Tom Henighan, Shauna Kravec, Zac Hatfield-Dodds, Robert Lasenby, Dawn Drain, Carol Chen, et al. Toy models of superposition. *arXiv preprint arXiv:2209.10652*, 2022. 2, 4
- [7] Ruth Fong, Mandela Patrick, and Andrea Vedaldi. Understanding deep networks via extremal perturbations and smooth masks. In *Proceedings of the IEEE/CVF international conference on computer vision*, pages 2950–2958, 2019. 1, 2, 3, 5
- [8] Ruth C Fong and Andrea Vedaldi. Interpretable explanations of black boxes by meaningful perturbation. In *Proceedings of the IEEE international conference on computer vision*, pages 3429–3437, 2017. 1, 2, 3
- [9] Kaiming He, Xiangyu Zhang, Shaoqing Ren, and Jian Sun. Deep residual learning for image recognition. In *Proceedings of the IEEE conference on computer vision and pattern recognition*, pages 770–778, 2016. 5
- [10] Andrew Ilyas, Shibani Santurkar, Dimitris Tsipras, Logan Engstrom, Brandon Tran, and Aleksander Madry. Adversarial examples are not bugs, they are features. *Advances in Neural Information Processing Systems*, 32, 2019. 2, 4
- [11] Hyungsik Jung and Youngrock Oh. Towards better explanations of class activation mapping. In *Proceedings of the IEEE/CVF international conference on computer vision*, pages 1336–1344, 2021. 2, 5
- [12] Andrei Kapishnikov, Subhashini Venugopalan, Besim Avci, Ben Wedin, Michael Terry, and Tolga Bolukbasi. Guided integrated gradients: An adaptive path method for removing noise. In *Proceedings of the IEEE/CVF conference on computer vision and pattern recognition*, pages 5050–5058, 2021. 2
- [13] Scott M Lundberg and Su-In Lee. A unified approach to interpreting model predictions. *Advances in neural information processing systems*, 30, 2017. 2
- [14] Chris Olah, Nick Cammarata, Ludwig Schubert, Gabriel Goh, Michael Petrov, and Shan Carter. Zoom in: An introduction to circuits. *Distill*, 5(3):e00024–001, 2020. 2, 4
- [15] Vitali Petsiuk, Abir Das, and Kate Saenko. Rise: Randomized input sampling for explanation of black-box models. *arXiv preprint arXiv:1806.07421*, 2018. 1, 2, 5
- [16] Changqing Qiu, Fusheng Jin, and Yining Zhang. Empowering cam-based methods with capability to generate fine-grained and high-faithfulness explanations. In *Proceedings of the AAAI Conference on Artificial Intelligence*, pages 4587–4595, 2024. 2
- [17] Olga Russakovsky, Jia Deng, Hao Su, Jonathan Krause, Sanjeev Satheesh, Sean Ma, Zhiheng Huang, Andrej Karpathy, Aditya Khosla, Michael Bernstein, Alexander C. Berg, and Li Fei-Fei. ImageNet Large Scale Visual Recognition Challenge. *International Journal of Computer Vision (IJCV)*, 115(3):211–252, 2015. 5
- [18] Wojciech Samek, Alexander Binder, Grégoire Montavon, Sebastian Lapuschkin, and Klaus-Robert Müller. Evaluating the visualization of what a deep neural network has learned. *IEEE transactions on neural networks and learning systems*, 28(11):2660–2673, 2016. 1, 2
- [19] Ramprasaath R Selvaraju, Michael Cogswell, Abhishek Das, Ramakrishna Vedantam, Devi Parikh, and Dhruv Batra. Grad-cam: Visual explanations from deep networks via gradient-based localization. In *Proceedings of the IEEE international conference on computer vision*, pages 618–626, 2017. 2, 5
- [20] Karen Simonyan and Andrew Zisserman. Very deep convolutional networks for large-scale image recognition. *arXiv preprint arXiv:1409.1556*, 2014. 5
- [21] Karen Simonyan, Andrea Vedaldi, and Andrew Zisserman. Deep inside convolutional networks: Visualising image classification models and saliency maps. *arXiv preprint arXiv:1312.6034*, 2013. 2, 5
- [22] Daniel Smilkov, Nikhil Thorat, Been Kim, Fernanda Viégas, and Martin Wattenberg. Smoothgrad: removing noise by adding noise. *arXiv preprint arXiv:1706.03825*, 2017. 2, 5
- [23] Jost Tobias Springenberg, Alexey Dosovitskiy, Thomas Brox, and Martin Riedmiller. Striving for simplicity: The all convolutional net. *arXiv preprint arXiv:1412.6806*, 2014. 2
- [24] Mukund Sundararajan, Ankur Taly, and Qiqi Yan. Axiomatic attribution for deep networks. In *International conference on machine learning*, pages 3319–3328. PMLR, 2017. 2, 5
- [25] Jorg Wagner, Jan Mathias Kohler, Tobias Gindele, Leon Hetzel, Jakob Thaddaus Wiedemer, and Sven Behnke. Interpretable and fine-grained visual explanations for convolutional neural networks. In *Proceedings of the IEEE/CVF Conference on Computer Vision and Pattern Recognition*, pages 9097–9107, 2019. 1, 2, 5
- [26] C. Wah, S. Branson, P. Welinder, P. Perona, and S. Belongie. The caltech-ucsd birds-200-2011 dataset. Technical Report CNS-TR-2011-001, California Institute of Technology, 2011. 5

- [27] Haofan Wang, Zifan Wang, Mengnan Du, Fan Yang, Zijian Zhang, Sirui Ding, Piotr Mardziel, and Xia Hu. Score-cam: Score-weighted visual explanations for convolutional neural networks. In *Proceedings of the IEEE/CVF conference on computer vision and pattern recognition workshops*, pages 24–25, 2020. [2](#), [5](#)
- [28] Kaidi Xu, Sijia Liu, Gaoyuan Zhang, Mengshu Sun, Pu Zhao, Quanfu Fan, Chuang Gan, and Xue Lin. Interpreting adversarial examples by activation promotion and suppression. *arXiv preprint arXiv:1904.02057*, 2019. [2](#), [4](#)
- [29] Matthew D Zeiler and Rob Fergus. Visualizing and understanding convolutional networks. In *European conference on computer vision*, pages 818–833. Springer, 2014. [2](#)
- [30] Lintong Zhang, Kang Yin, and Seong-Whan Lee. Towards fine-grained interpretability: Counterfactual explanations for misclassification with saliency partition. In *Proceedings of the Computer Vision and Pattern Recognition Conference*, pages 30053–30062, 2025. [2](#), [5](#)
- [31] Bolei Zhou, Aditya Khosla, Agata Lapedriza, Aude Oliva, and Antonio Torralba. Learning deep features for discriminative localization. In *Proceedings of the IEEE conference on computer vision and pattern recognition*, pages 2921–2929, 2016. [2](#)

# Beyond Output Faithfulness: Learning Attributions that Preserve Computational Pathways

## Supplementary Material

Table 4. **Ablation Study** on ImageNet with VGG16 using FEI<sub>VM</sub>.

Configuration	Ins.↑	Del.↓	MSE↓	Cosine.↑
<b>FEI<sub>VM</sub> (full method)</b>	0.512	0.117	0.545	0.688
<i>Quantile levels</i>				
(0.1, 0.5, 0.9)	0.509	0.107	0.568	0.683
(0.1, 0.2, ..., 0.9)	0.532	0.125	0.547	0.690
<i>Regularization schedule (<math>\beta</math>)</i>				
Constant ( $\beta = 10^0$ )	0.513	0.113	0.550	0.688
Constant ( $\beta = 10^{-2}$ )	0.500	0.131	0.543	0.680
Constant ( $\beta = 10^{-3}$ )	0.339	0.148	0.785	0.526
<i>Gradient clipping scope</i>				
Early layers only (1-4)	0.550	0.114	0.610	0.664
Early layers only (1-8)	0.544	0.113	0.584	0.673
Early layers only (1-16)	0.525	0.113	0.559	0.681
Later layers only (16-30)	0.430	0.069	0.717	0.603
<i>Area Regulation</i>				
L1( $\beta = 1e^{-1}$ )	0.328	0.226	0.794	0.486
L1( $\beta = 1e^{-2}$ )	0.464	0.147	0.576	0.648
L1( $\beta = 1e^{-3}$ )	0.213	0.102	1.016	0.392
No Constraint	0.127	0.156	1.118	0.290
<i>Optimization Step</i>				
epochs(300)	0.518	0.129	0.521	0.693
epochs(200)	0.516	0.125	0.527	0.692
epochs(50)	0.491	0.088	0.624	0.663

## A. Ablation Studies

We conduct comprehensive ablation experiments to validate the design choices in our Faithfulness-guided Ensemble Interpretation (FEI) framework. All experiments are performed on ImageNet with VGG16 using the FEI<sub>VM</sub> variant. Unless otherwise specified, the baseline configuration uses:  $\beta = 0.1$ , 100 optimization iterations per quantile, quantile levels  $\mathcal{Q} = \{0.1, 0.3, 0.5, 0.7, 0.9\}$ , and gradient clipping applied to all convolutional layers. Results are presented in Table 4.

### A.1. Quantile Level Selection

We investigate the impact of quantile granularity on explanation quality. Our default configuration uses five quantile levels  $\{0.1, 0.3, 0.5, 0.7, 0.9\}$ , balancing computational cost with curve coverage.

**Fewer quantiles** ( $\{0.1, 0.5, 0.9\}$ ): Using only three quantile levels achieves comparable performance (Ins.: 0.509, Del.: 0.107, MSE: 0.568, Cosine: 0.683) with reduced computational cost.

**More quantiles** ( $\{0.1, 0.2, \dots, 0.9\}$ ): Increasing to nine quantile levels yields similar results (Ins.: 0.532, Del.: 0.125, MSE: 0.547, Cosine: 0.690) with proportionally increased computation time.

**Conclusion:** The small performance gap between three,

five, and nine quantile levels (insertion scores within 0.023, internal faithfulness metrics within 0.021 MSE and 0.007 cosine similarity) demonstrates the robustness of our method to quantile granularity. Five quantile levels provide a reasonable default, though practitioners can adjust based on computational budgets without significant quality degradation.

### A.2. Regularization Strength ( $\beta$ )

The constraint penalty weight  $\beta$  in Equation 5 enforces the quantile constraint (Equation 3). We examine different magnitudes to determine sufficient constraint strength.

**Strong regularization** ( $\beta = 10^0 = 1.0$ ): High penalty weight maintains comparable performance (Ins.: 0.513, Del.: 0.113, MSE: 0.550, Cosine: 0.688) to our default  $\beta = 0.1$ , confirming sufficient constraint enforcement.

**Moderate regularization** ( $\beta = 10^{-2} = 0.01$ ): Reducing  $\beta$  to 0.01 shows slight degradation (Ins.: 0.500, Del.: 0.131, Cosine: 0.680), indicating the constraint becomes under-enforced.

**Weak regularization** ( $\beta = 10^{-3} = 0.001$ ): Further reduction causes catastrophic failure—insertion drops to 0.339, MSE increases to 0.785, and cosine similarity degrades to 0.526. Without sufficient constraint enforcement, the optimization produces invalid attribution maps that violate the quantile-based masking assumption.

**Conclusion:** We only need  $\beta$  to be large enough to ensure the quantile constraint is always fulfilled during optimization. The results show that  $\beta = 0.1$  is sufficiently large, as increasing it to 1.0 provides no additional benefit. The sharp degradation at  $\beta = 10^{-3}$  confirms that inadequate constraint enforcement leads to optimization failure.

### A.3. Ensemble Quantile Optimization vs. Area Regularization

To validate our choice of Ensemble Quantile Optimization (EQO) over simpler area-based regularization, we replace the quantile-based objective with a direct L1 penalty on attribution area:  $\mathcal{L} = -\phi(\tilde{x}) + \beta\|\alpha\|_1$ . This approximates sparsity-based methods like Extremal Perturbation [7].

**L1 regularization across  $\beta$  values:** All L1 configurations perform substantially worse than EQO:

- At  $\beta = 10^{-1}$ : Ins. 0.328 (vs. 0.512 for EQO), MSE 0.794 (vs. 0.545)
- At  $\beta = 10^{-2}$ : Ins. 0.464, still significantly below EQO baseline



Figure 5. Ablation Study: Impact of Layer Clipping Ranges on Visual Explanations

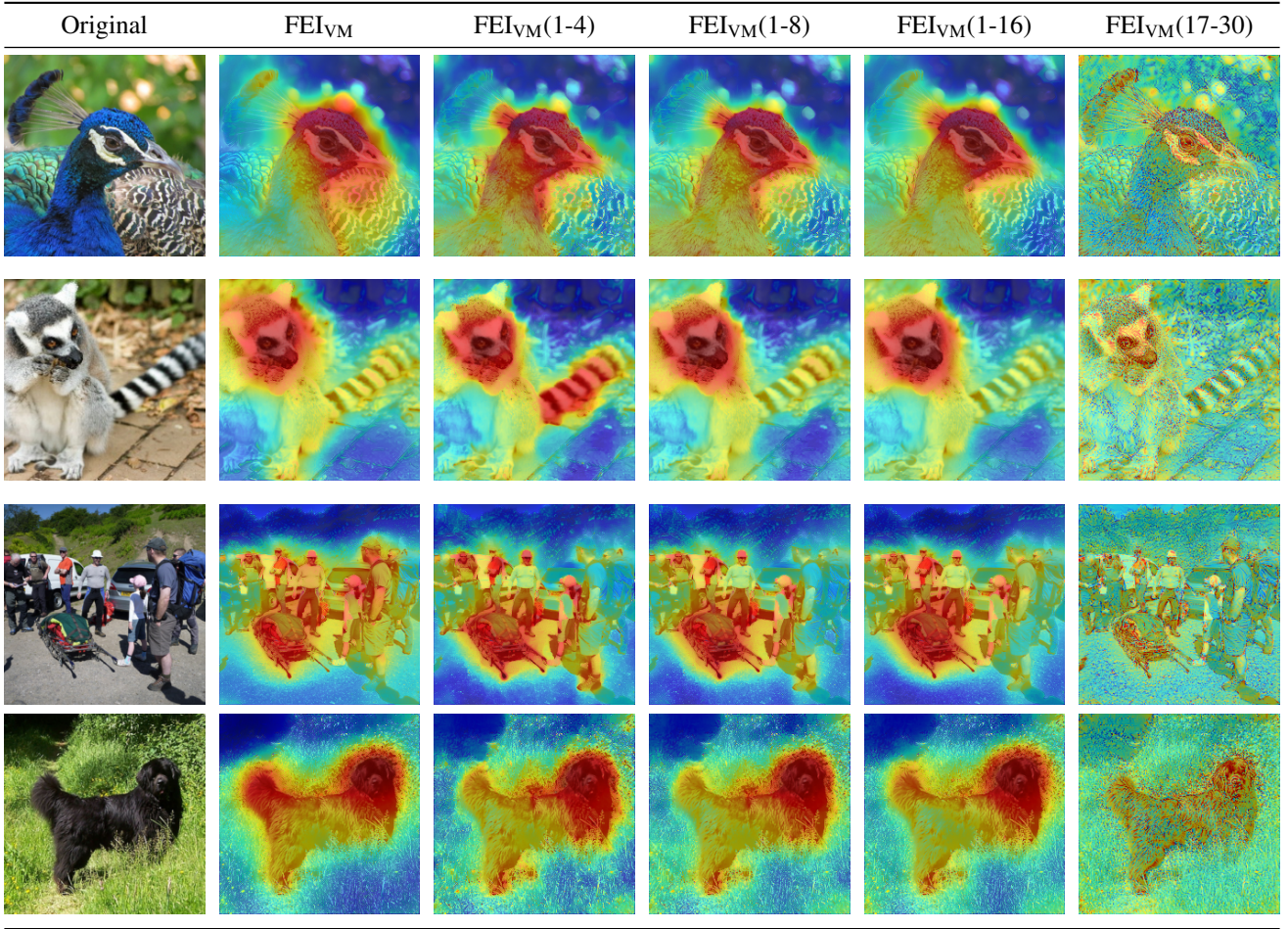


Figure 6. The ablation visualization of different clipping choices

- At  $\beta = 10^{-3}$ : Catastrophic failure with Ins. 0.213, MSE 1.016, Cosine 0.392

**No constraint baseline:** We also include a special case where no area regularization is applied ( $\beta = 0$ ). This configuration, which optimizes  $-\phi(\tilde{x})$  while still using VM clipping, fails to find a meaningful attribution (Ins.: 0.127, MSE: 1.118, Cosine: 0.290). This demonstrates that a strong regularization signal—either a sparsity prior like L1 or a curve-based constraint like EQO—is essential for the optimization to discover a salient, compact explanation.

**Conclusion:** EQO shows clear supremacy over simple L1 area regularization. The explicit modeling of the full insertion curve provides substantially richer gradient information than surrogate sparsity objectives, leading to consistent improvements across all metrics (external and internal faithfulness).

#### A.4. Optimization Iterations

We examine convergence behavior by varying the number of optimization iterations per quantile level.

**Extended optimization** (200–300 iterations): Increasing iterations to 200 or 300 provides marginal improvements (Ins.: 0.516–0.518, MSE: 0.521–0.527, Cosine: 0.692–0.693) compared to the baseline 100 iterations, indicating performance saturation.

**Reduced optimization** (50 iterations): Halving the optimization budget to 50 iterations degrades both external faithfulness (Ins.: 0.491, Del.: 0.088) and internal preservation (MSE: 0.624, Cosine: 0.663), indicating insufficient convergence.

**Conclusion:** Our default of 100 iterations per quantile level provides a strong balance between computational cost and explanation quality. Performance saturates around 100–200 iterations, with diminishing returns beyond this range.



## A.5. Gradient Clipping Scope

A key question is whether activation preservation constraints should be applied globally or selectively to specific network regions. We compare constraining early layers only, late layers only, or all layers (default).

**Early layers only:** Constraining progressively more early layers (1–4, 1–8, 1–16) reveals an interesting cascade effect. As shown in Table 4, constraining layers 1–4 yields the highest insertion score (0.550) but moderate internal faithfulness (MSE: 0.610, Cosine: 0.664). Extending constraints to layers 1–8 (Ins.: 0.544, MSE: 0.584) and 1–16 (Ins.: 0.525, MSE: 0.559) progressively improves activation preservation while maintaining competitive external performance.

**Later layers only (16–30):** Constraining only late layers produces a striking failure pattern—while achieving the lowest deletion score (0.069), insertion performance collapses to 0.430 and internal faithfulness degrades substantially (MSE: 0.717, Cosine: 0.603). This demonstrates that constraining earlier layers is better than constraining later layers due to the cascading effect: early-layer deviations propagate and amplify through the forward pass, ultimately disrupting later-layer activations even when those layers are directly constrained.

**Comparison with full clipping:** Compared to our default configuration (all layers, Ins.: 0.512, MSE: 0.545), early layer clipping (1–16) provides a slightly better external score (0.525) since it is less constrained during optimization. However, it does have slightly worse activation preservation scores (MSE: 0.559 vs. 0.545, Cosine: 0.681 vs. 0.688), confirming the expected trade-off between optimization flexibility and internal consistency.

**Qualitative analysis:** Figure 6 visualizes attribution maps across different clipping strategies. Early layer clipping (1–16) does not degrade visualization quality—the attributions remain coherent and object-focused, similar to full clipping. In contrast, later layer clipping (16–30) makes the attributions much worse, producing diffuse, noisy maps that fail to capture meaningful object structures. This qualitative finding aligns with our quantitative results and confirms that early-layer constraint is essential for pathway preservation.

**Conclusion:** The cascade effect reveals that activation pathway preservation must begin at the network’s earliest layers. Constraining only later layers is insufficient because unconstrained early deviations compound through the network. While early-layer-only clipping (1–16) offers a practical compromise with slightly better external scores and acceptable internal faithfulness, our default configuration of constraining all convolutional layers achieves the best overall balance and most robust pathway preservation.

## B. Architectural Sensitivity

While ClipGrad implementation is architecture-agnostic, the *interaction* between constraint types and architectural motifs reveals systematic patterns that guide variant selection. We analyze how multi-branch connections and sequential depth modulate the constraint-expressivity trade-off.

### B.1. Constraint Propagation in Sequential vs. Multi-Branch Architectures

Sequential architectures exhibit unidirectional information flow where each layer’s output becomes the next layer’s input (see Eq. (7)). Constraint violations at early layers propagate forward without correction mechanisms. In contrast, multi-branch architectures incorporate skip connections that provide compensatory pathways. For ResNet blocks:

$$h_{\ell+1} = \text{ReLU}(f_{\ell}^{\text{residual}}(h_{\ell}) + h_{\ell}) \quad (12)$$

This additive structure enables the network to absorb and redistribute activation perturbations caused by gradient constraints.

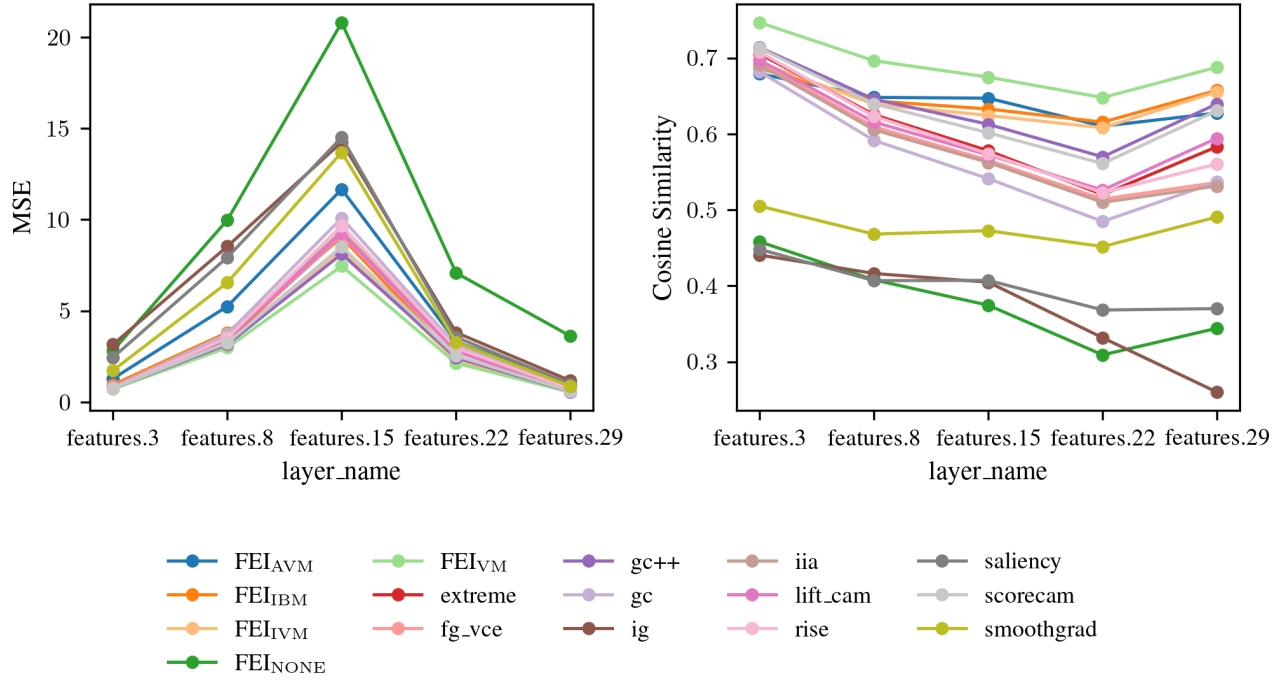
### B.2. AVM: Asymmetric Constraint on Activation Decreases

$\text{FEI}_{\text{AVM}}$  prevents active neurons from deactivating while permitting new neuron activation (Eq. (10)). In sequential networks without compensatory mechanisms, this constraint causes progressive activation accumulation across depth. At layer  $\ell$ , AVM blocks gradients that would reduce  $\tilde{h}^{\ell}[i]$  below  $h^{\ell}[i]$ . Layer  $\ell + 1$  then receives these elevated inputs and produces higher activations. This cascade effect means each subsequent layer inherits and amplifies these deviations, manifesting as sharper, edge-emphasized attribution maps (Fig. 3) and catastrophic failure on blank images with 91.8% spurious attribution rate on AlexNet and 94.1% on VGG16 (Tab. 2).

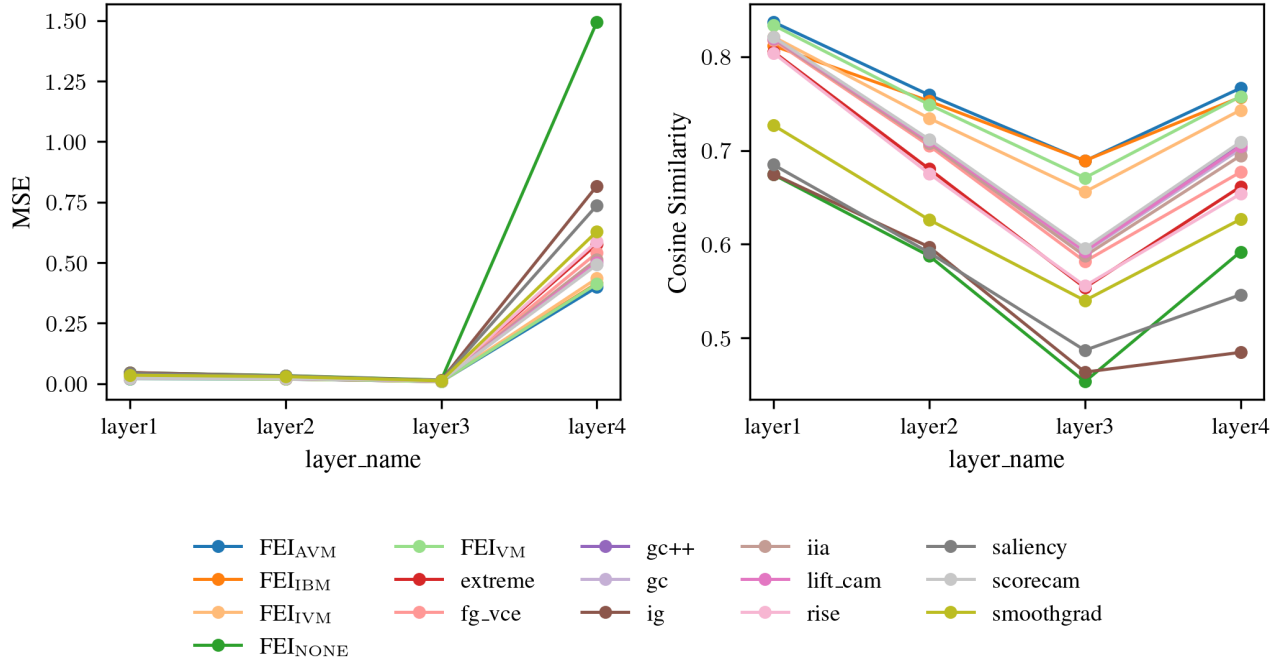
In multi-branch networks, skip connections provide three stabilization mechanisms. First, gradient clipping only affects the residual branch, not the skip pathway, localizing the constraint’s impact. Second, the addition operation  $h_{\ell+1} = \text{ReLU}(f_{\ell}^{\text{res}}(h_{\ell}) + h_{\ell})$  dilutes elevated residual activations by averaging them with original skip activations. Third, the post-addition ReLU provides nonlinear gating that re-normalizes the combined signal, preventing unbounded growth. These mechanisms produce stable activation flow with smooth, coherent attributions and near-zero failure rates (0.1% on ResNet50/GoogLeNet, Tab. 2).

### B.3. IBM/IVM: Asymmetric Constraint on Activation Increases

$\text{FEI}_{\text{IBM}}$  and  $\text{FEI}_{\text{IVM}}$  prevent spurious neuron activation (Eq. (11)). By suppressing activation increases rather than

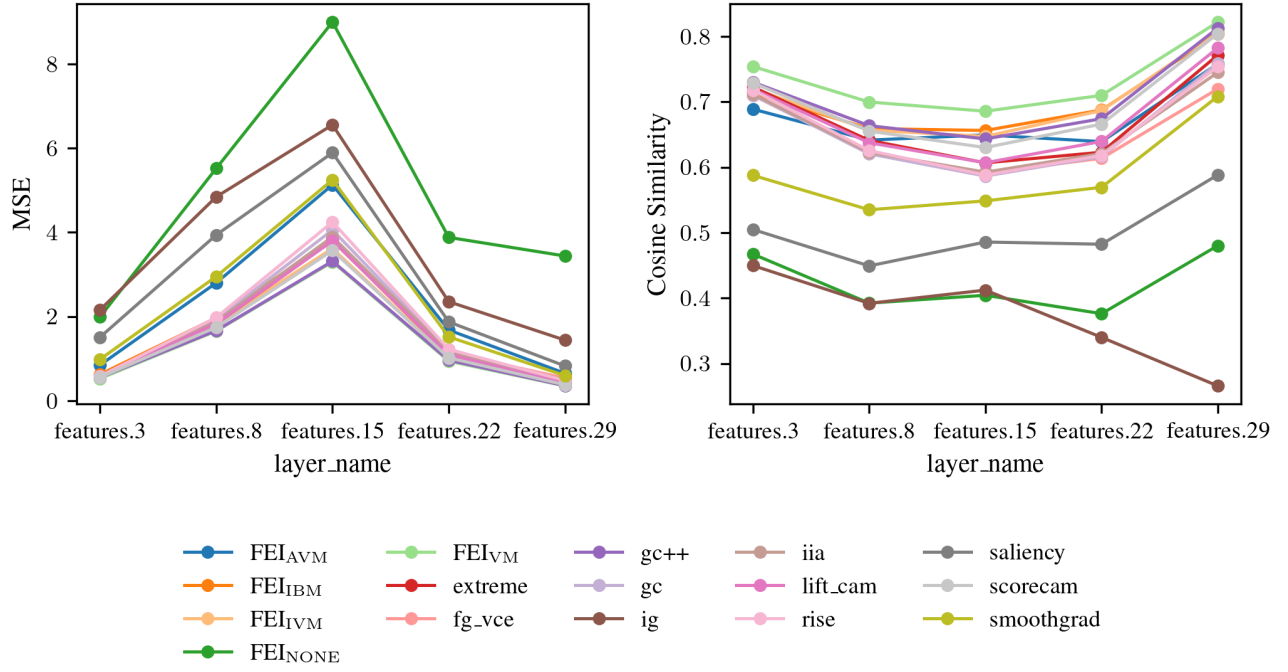


(a) VGG16-ImageNet

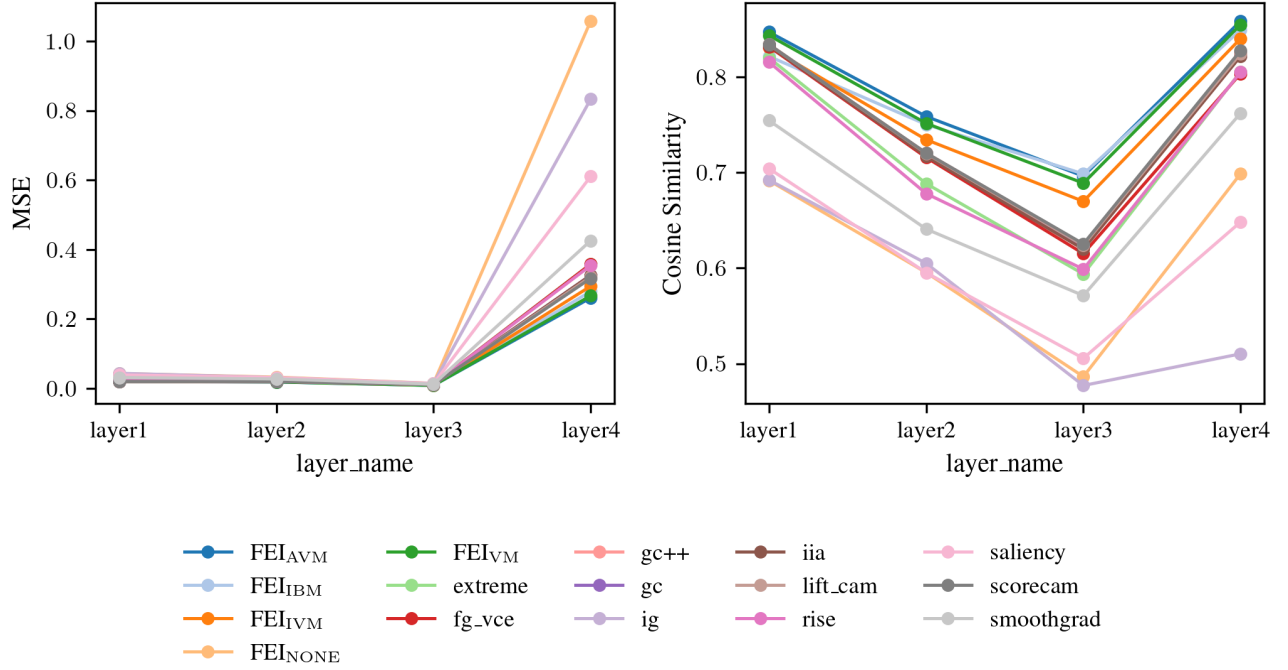


(b) ResNet50-ImageNet

Figure 7. Layer-wise internal faithfulness metrics on additional architecture-dataset combinations. MSE (lower is better) measures activation magnitude deviation, while Pearson correlation (higher is better) captures structural similarity. Consistent with the main paper (Fig. 2a), gradient-based methods and FEI<sub>NONE</sub> exhibit significantly worse preservation compared to FEI variants with internal constraints across all settings. (Continued on next page)



(c) VGG16-CUB-200-2011



(d) ResNet50-CUB-200-2011

Figure 7. (Continued) Layer-wise internal faithfulness metrics.

decreases, these variants avoid the accumulation problem entirely. In sequential networks, direct suppression prevents uncontrolled activation spread, producing precise, localized

attribution maps. In multi-branch networks, skip connections soften the constraint effect, yielding more diffuse but semantically stable attributions. Both variants achieve ro-

Table 5. Layer-wise internal activation matching on ResNet50 across ImageNet and CUB-200-2011. Lower MSE and higher cosine similarity indicate better internal faithfulness. MSE values remain compressed in early layers (Layer1–3) but differences become pronounced in Layer4, consistent with Fig. 7. The pattern holds across both datasets, confirming the BatchNorm stabilization effect.

Method	ImageNet								CUB-200-2011							
	MSE ↓				Cosine ↑				MSE ↓				Cosine ↑			
	L1	L2	L3	L4	L1	L2	L3	L4	L1	L2	L3	L4	L1	L2	L3	L4
GradCAM++	.021	.021	.011	.495	.820	.711	.595	.708	.020	.020	.011	.320	.834	.720	.625	.826
ScoreCAM	.021	.021	.011	.491	.821	.712	.596	.709	.021	.020	.011	.317	.834	.721	.625	.828
Lift-CAM	.021	.021	.011	.500	.820	.710	.593	.704	.021	.020	.011	.322	.834	.720	.624	.825
GradCAM	.021	.021	.011	.505	.820	.709	.591	.701	.021	.020	.011	.326	.834	.719	.623	.822
FG-VCE	.022	.021	.011	.540	.817	.705	.582	.677	.021	.020	.011	.358	.832	.716	.615	.804
IIA	.022	.021	.011	.514	.819	.708	.588	.694	.021	.020	.011	.326	.833	.717	.620	.822
RISE	.024	.025	.012	.588	.804	.675	.556	.654	.023	.024	.012	.354	.816	.678	.599	.805
Extremal Perturbation	.023	.024	.012	.577	.805	.680	.554	.661	.022	.023	.012	.358	.820	.688	.594	.805
SmoothGrad	.035	.029	.012	.629	.727	.626	.540	.627	.032	.027	.012	.426	.754	.641	.571	.762
Saliency	.042	.032	.013	.736	.685	.591	.487	.546	.039	.031	.014	.611	.704	.595	.506	.648
Integrated Gradients	.046	.032	.014	.817	.675	.597	.464	.485	.044	.031	.015	.833	.692	.605	.477	.510
FEI <sub>VM</sub>	<b>.021</b>	<u>.019</u>	<u>.009</u>	<u>.412</u>	<u>.833</u>	<u>.749</u>	<u>.671</u>	<u>.758</u>	<u>.019</u>	<u>.019</u>	<u>.009</u>	<u>.267</u>	<u>.844</u>	<u>.752</u>	<u>.689</u>	<u>.855</u>
FEI <sub>IVM</sub>	.022	.020	.009	.435	.821	.734	.656	.743	.021	.020	.009	.295	.831	.734	.670	.840
FEI <sub>IBM</sub>	.024	.019	<b>.008</b>	.415	.812	.753	<b>.689</b>	.757	.023	.020	<b>.009</b>	.280	.822	.750	<b>.699</b>	.849
FEI <sub>AVM</sub>	<u>.021</u>	<b>.019</b>	.009	<b>.399</b>	<b>.837</b>	<b>.759</b>	<u>.689</u>	<b>.766</b>	<b>.020</b>	<b>.019</b>	.009	<b>.261</b>	<b>.847</b>	<b>.759</b>	.696	<b>.859</b>
FEI <sub>NONE</sub>	.045	.033	.015	1.494	.674	.588	.454	.592	.043	.033	.015	1.058	.692	.595	.486	.699

Table 6. Layer-wise internal activation matching on VGG16 across ImageNet and CUB-200-2011. Lower MSE and higher cosine similarity indicate better internal faithfulness. MSE values remain compressed in early layers (features.3–15) but differences become pronounced in later layers (features.22–29), consistent with the feature hierarchy. Best results in **bold**, second-best underlined.

Method	ImageNet										CUB-200-2011									
	MSE ↓					Cosine ↑					MSE ↓					Cosine ↑				
	F3	F8	F15	F22	F29	F3	F8	F15	F22	F29	F3	F8	F15	F22	F29	F3	F8	F15	F22	F29
GradCAM++	0.762	<u>3.165</u>	<u>8.116</u>	2.438	0.573	<u>.714</u>	.646	.613	.570	.640	0.549	1.664	<u>3.315</u>	<u>0.960</u>	<u>0.355</u>	<u>.730</u>	<u>.664</u>	.643	.674	<u>.813</u>
ScoreCAM	0.763	3.254	8.520	2.544	0.588	.713	.640	.602	.561	.631	0.553	1.743	3.567	1.017	0.376	.729	.655	.630	.666	.804
Lift-CAM	0.799	3.483	9.245	2.786	0.648	.697	.616	.572	.526	.594	0.568	1.830	3.799	1.093	0.410	.719	.637	.607	.639	.783
GradCAM	0.834	3.729	10.087	3.100	0.755	.682	.592	.541	.485	.537	0.585	1.929	4.055	1.179	0.461	.710	.621	.587	.616	.759
FG-VCE	0.805	3.472	9.132	2.773	0.742	.693	.609	.565	.514	.536	0.580	1.852	3.818	1.145	0.535	.710	.623	.591	.614	.720
IIA	0.813	3.538	9.372	2.915	0.765	.691	.605	.563	.510	.531	0.579	1.879	3.892	1.156	0.491	.712	.623	.592	.621	.745
RISE	0.784	3.531	9.672	2.970	0.731	.708	.623	.574	.523	.561	0.577	1.976	4.245	1.220	0.478	.718	.625	.588	.618	.754
Extremal Perturbation	0.784	3.423	9.123	2.790	0.671	.706	.625	.578	.520	.583	0.564	1.827	3.804	1.133	0.436	.723	.641	.607	.623	.772
SmoothGrad	1.733	6.550	13.692	3.284	0.862	.505	.468	.473	.452	.491	0.982	2.949	5.245	1.516	0.596	.588	.535	.549	.569	.708
Saliency	2.451	7.936	14.510	3.561	0.984	.448	.407	.407	.368	.370	1.507	3.937	5.890	1.871	0.824	.505	.449	.486	.482	.588
Integrated Gradients	3.164	8.533	14.252	3.816	1.173	.441	.416	.405	.332	.260	2.157	4.842	6.552	2.351	1.438	.450	.392	.412	.340	.266
FEI <sub>VM</sub>	<b>0.717</b>	<b>2.986</b>	<b>7.455</b>	<b>2.134</b>	<b>0.545</b>	<b>.747</b>	<b>.696</b>	<b>.675</b>	<b>.648</b>	<b>.688</b>	<b>0.525</b>	<b>1.654</b>	<b>3.295</b>	<b>0.938</b>	<b>0.349</b>	<b>.754</b>	<b>.700</b>	<b>.686</b>	<b>.710</b>	<b>.822</b>
FEI <sub>IVM</sub>	0.840	3.418	8.344	<u>2.284</u>	<u>0.567</u>	.694	.639	.624	.608	.656	0.579	1.824	3.617	1.000	0.371	.720	.657	.647	.687	.807
FEI <sub>IBM</sub>	0.953	3.817	9.030	2.417	0.629	.686	.644	.633	<u>.616</u>	<u>.658</u>	0.625	1.968	3.817	1.061	0.402	.713	.659	<u>.656</u>	<u>.688</u>	.804
FEI <sub>AVM</sub>	1.291	5.247	11.666	3.313	0.952	.679	<u>.648</u>	<u>.647</u>	.610	<u>.628</u>	0.845	2.799	5.129	1.679	0.649	.689	.641	<u>.649</u>	.639	.758
FEI <sub>NONE</sub>	2.823	9.981	20.796	7.081	3.619	.458	.408	.374	.309	.344	1.991	5.518	8.996	3.878	3.437	.467	.392	.404	.376	.480

bust performance across architectures with 0–0.2% failure rates (Tab. 2).

#### B.4. VM: Bidirectional Constraint

FEI<sub>VM</sub> enforces strict activation equality by blocking both increases and decreases (Eq. (8)). This symmetric con-

straint prevents accumulation in both directions, providing robustness independent of architectural topology with 0.1% failure rate across all architectures (Tab. 2).



## B.5. Practical Guidance

For maximal robustness across architectures,  $\text{FEI}_{\text{VM}}$  is the recommended default, enforcing strict activation equality regardless of topology. For architecture-specific tuning, we recommend  $\text{FEI}_{\text{IBM}}$  or  $\text{FEI}_{\text{IVM}}$  for sequential networks (VGG, AlexNet) to prevent activation spread, and  $\text{FEI}_{\text{AVM}}$  for multi-branch networks (ResNet, Inception) where skip connections stabilize attribution flow.

The selection ultimately depends on priorities:  $\text{FEI}_{\text{VM}}$  for robustness (0.1% failure rate across all architectures),  $\text{FEI}_{\text{IBM}}$  for optimal external faithfulness (best insertion scores, Tab. 1), and  $\text{FEI}_{\text{AVM}}$  for visual quality on multi-branch architectures or  $\text{FEI}_{\text{VM}}$  on sequential ones (Fig. 3).

## C. Layer-wise Internal Faithfulness Analysis

Figure 7 demonstrates consistent patterns across all architecture-dataset combinations. Gradient-based methods and  $\text{FEI}_{\text{NONE}}$  form distinct outliers with substantially higher MSE and lower correlation compared to other attribution methods.

**ResNet50-specific patterns.** The MSE profiles in Fig. 7 appear visually compressed in ResNet50’s early layers compared to VGG16, making differences less apparent in the plots. However, Tab. 5 reveals the underlying trends quantitatively. In early layers (Layer1–3), MSE values remain tightly clustered, with gradient-based methods showing only modest elevation. This compression stems from batch normalization’s stabilizing effect—BatchNorm layers throughout the network constrain activation magnitudes by normalizing feature statistics within each mini-batch.

The final layer (Layer4) exhibits a dramatic shift. MSE values increase by an order of magnitude, and method differences become pronounced. Constrained FEI variants maintain low MSE, while gradient-based methods degrade significantly, and  $\text{FEI}_{\text{NONE}}$  shows catastrophic failure. This pattern reflects a fundamental architectural trade-off: BatchNorm stabilizes representations throughout the network for training efficiency, but the final feature layer must preserve sufficient discriminative magnitude to enable the classification head to separate classes effectively. When perturbations occur at this critical juncture without internal constraints, the disruption to these discriminative activations becomes severe.

**Cross-dataset consistency.** Despite CUB-200-2011’s fine-grained classification task versus ImageNet’s broader categorization, the layer-wise patterns remain remarkably consistent (Tab. 5). Both datasets show: (1) compressed early-layer MSE maintained by BatchNorm, (2) dramatic Layer4 MSE increase reflecting discriminative requirements, and (3) superior preservation by constrained FEI variants.

**Implications for evaluation.** This analysis demon-

strates that while Fig. 7 provides intuitive visualization of preservation trends, the compressed scale in ResNet50’s early layers can obscure method differences. The numerical precision in Tab. 5 confirms that gradient-based methods and  $\text{FEI}_{\text{NONE}}$  consistently deviate from the model’s computational pathway across all layers, even when visual differences appear subtle. Methods without internal constraints consistently fail to preserve the model’s computational pathway, while constrained FEI variants maintain activation consistency across layers, architectures, and datasets.

## D. Derivation of Selective Gradient Clipping (ClipGrad) Variants

The Selective Gradient Clipping (ClipGrad) operations are derived from a unified loss function that combines external and internal faithfulness objectives.

### D.1. Value Matching (VM) Variants

We define the total loss as:

$$\mathcal{L}_{\text{total}} = \mathcal{L}_{\text{ins}} + \mathcal{L}_{\text{int}} \quad (13)$$

The external gradient is:

$$\gamma_h = \frac{\partial \mathcal{L}_{\text{ins}}}{\partial \tilde{h}^\ell} \quad (14)$$

The internal loss is designed to match the relevant parts of internal activations, where relevance is measured by saliency:

$$\mathcal{L}_{\text{int}} = \beta_{\text{int}} \sum_i M^\ell[i] \cdot d(h^\ell[i], \tilde{h}^\ell[i]) \quad (15)$$

where:

- $M^\ell[i]$  is the saliency (relevance) of neuron  $i$  at layer  $\ell$
- $d(h^\ell[i], \tilde{h}^\ell[i])$  is a distance function measuring deviation from the original activation
- $\beta_{\text{int}}$  is a balancing coefficient

We make two assumptions:

1. Distance function:  $d(x, y) = |x - y|$  (L1 distance)
2. Saliency approximation:  $M[i] \approx |\gamma_h[i]|$

This yields the internal loss:

$$\mathcal{L}_{\text{int}} = \beta_{\text{int}} \sum_i |\gamma_h[i]| \cdot |h^\ell[i] - \tilde{h}^\ell[i]| \quad (16)$$

The gradient of the internal loss is:

$$\frac{\partial \mathcal{L}_{\text{int}}}{\partial \tilde{h}^\ell[i]} = \beta_{\text{int}} \cdot |\gamma_h[i]| \cdot \text{sign}(\tilde{h}^\ell[i] - h^\ell[i]) \quad (17)$$

The total gradient is:

$$\tilde{\gamma}_h[i] = \gamma_h[i] + \beta_{\text{int}} \cdot |\gamma_h[i]| \cdot \text{sign}(\tilde{h}^\ell[i] - h^\ell[i]) \quad (18)$$

### Derivation of Value Matching (VM)

Setting  $\beta_{\text{int}} = 1$  and expanding by cases:

$$\tilde{\gamma}_h[i] = \begin{cases} \gamma_h[i] + \gamma_h[i] \cdot (+1) = 2\gamma_h[i] & \text{if } \gamma_h[i] > 0 \\ & \wedge \tilde{h}^\ell[i] > h^\ell[i] \\ \gamma_h[i] + |\gamma_h[i]| \cdot (-1) = 2\gamma_h[i] & \text{if } \gamma_h[i] \leq 0 \\ & \wedge \tilde{h}^\ell[i] \leq h^\ell[i] \\ \gamma_h[i] + \gamma_h[i] \cdot (-1) = 0 & \text{if } \gamma_h[i] > 0 \\ & \wedge \tilde{h}^\ell[i] \leq h^\ell[i] \\ \gamma_h[i] + |\gamma_h[i]| \cdot (+1) = 0 & \text{if } \gamma_h[i] \leq 0 \\ & \wedge \tilde{h}^\ell[i] > h^\ell[i] \end{cases} \quad (19)$$

Absorbing the factor of 2 into the learning rate, we obtain the

$$\tilde{\gamma}_h[i] = \begin{cases} 0 & \text{if } (\gamma_h[i] \leq 0 \wedge \tilde{h}^\ell[i] > h^\ell[i]) \\ & \vee (\gamma_h[i] > 0 \wedge \tilde{h}^\ell[i] \leq h^\ell[i]) \\ \gamma_h[i] & \text{otherwise.} \end{cases} \quad (20)$$

**Analysis.** VM clips the gradient whenever the external objective pushes  $\tilde{h}^\ell[i]$  away from the original value  $h^\ell[i]$ . Notably, while the derivation begins with a saliency-weighted loss (Eq. 15), the resulting clipping rule (Eq. 19) is binary and independent of the gradient's magnitude. This final algorithm aligns with our MI argument by treating all neurons as part of the computational pathway, enforcing strict bidirectional preservation of activation patterns.

In gradient descent ( $\tilde{h}^\ell \leftarrow \tilde{h}^\ell - \alpha \tilde{\gamma}_h$ ):

- When  $\gamma_h[i] > 0$  and  $\tilde{h}^\ell[i] \leq h^\ell[i]$ : The optimizer wants to decrease  $\tilde{h}^\ell[i]$ , but it is already at or below  $h^\ell[i]$ . Clipping prevents further suppression.
- When  $\gamma_h[i] \leq 0$  and  $\tilde{h}^\ell[i] > h^\ell[i]$ : The optimizer wants to increase  $\tilde{h}^\ell[i]$ , but it is already above  $h^\ell[i]$ . Clipping prevents spurious amplification.

### Derivation of Activated Value Matching (AVM)

AVM uses only Case 3 from the VM derivation:

$$\tilde{\gamma}_h[i] = \begin{cases} 0 & \text{if } \gamma_h[i] > 0 \wedge \tilde{h}^\ell[i] \leq h^\ell[i] \\ \gamma_h[i] & \text{otherwise.} \end{cases} \quad (21)$$

**Analysis.** AVM prevents suppression of activations below their original values. It blocks gradient descent when  $\gamma_h[i] > 0$  (wants to decrease) and  $\tilde{h}^\ell[i] \leq h^\ell[i]$  (already at or below original). This allows increases but prevents further suppression of already-suppressed neurons.

### Derivation of Inactivated Value Matching (IVM)

IVM uses only Case 4 from the VM derivation:

$$\tilde{\gamma}_h[i] = \begin{cases} 0 & \text{if } \gamma_h[i] \leq 0 \wedge \tilde{h}^\ell[i] > h^\ell[i] \\ \gamma_h[i] & \text{otherwise.} \end{cases} \quad (22)$$

**Analysis.** IVM prevents spurious increases of activations above their original values. It blocks gradient descent when

$\gamma_h[i] \leq 0$  (wants to increase) and  $\tilde{h}^\ell[i] > h^\ell[i]$  (already above original). This allows decreases but prevents further amplification of already-amplified neurons.

## D.2. Binary Matching (BM) Variants

The **Binary Matching** variants are derived from a binary-aware distance function that matches only the *sign* of the activation rather than its exact value.

### Binary Distance Function

Instead of the  $L_1$  distance used for VM, we define a binary-aware distance function:

$$d(h^\ell[i], \tilde{h}^\ell[i]) = (1 - B(h^\ell[i]))(\tilde{h}^\ell[i] - h^\ell[i]) + \quad (23)$$

$$B(h^\ell[i])(h^\ell[i] - \tilde{h}^\ell[i]) \quad (24)$$

where  $B(h^\ell[i])$  is a binary indicator:

$$B(h^\ell[i]) = \begin{cases} 0 & \text{if } h^\ell[i] \leq 0 \text{ (inactive)} \\ 1 & \text{if } h^\ell[i] > 0 \text{ (active)} \end{cases} \quad (25)$$

The total gradient becomes:

$$\tilde{\gamma}_h[i] = \gamma_h[i] + |\gamma_h[i]| \cdot (1 - 2B(h^\ell[i])) \quad (26)$$

### Derivation of Binary Matching (BM)

Setting  $\beta_{\text{int}} = 1$ , we have

$$\tilde{\gamma}_h[i] = \begin{cases} \gamma_h[i] + |\gamma_h[i]| = 0 & \text{if } \gamma_h[i] \leq 0 \wedge h^\ell[i] \leq 0 \\ \gamma_h[i] + |\gamma_h[i]| = 2\gamma_h[i] & \text{if } \gamma_h[i] > 0 \wedge h^\ell[i] \leq 0 \\ \gamma_h[i] - |\gamma_h[i]| = 2\gamma_h[i] & \text{if } \gamma_h[i] \leq 0 \wedge h^\ell[i] > 0 \\ \gamma_h[i] - |\gamma_h[i]| = 0 & \text{if } \gamma_h[i] > 0 \wedge h^\ell[i] > 0 \end{cases} \quad (27)$$

Absorbing the factor of 2 into the learning rate, we obtain the **Binary Matching (BM)** rule:

$$\tilde{\gamma}_h[i] = \begin{cases} 0 & \text{if } (\gamma_h[i] \leq 0 \wedge h^\ell[i] \leq 0) \\ & \vee (\gamma_h[i] > 0 \wedge h^\ell[i] > 0) \\ \gamma_h[i] & \text{otherwise} \end{cases} \quad (28)$$

**Analysis.** BM clips the gradient in two scenarios:

- When  $\gamma_h[i] \leq 0$  and  $h^\ell[i] \leq 0$ : The optimizer wants to increase an inactive neuron. Clipping prevents spurious activation.
- When  $\gamma_h[i] > 0$  and  $h^\ell[i] > 0$ : The optimizer wants to decrease an active neuron. Clipping prevents spurious deactivation.

BM enforces binary state preservation: inactive neurons stay inactive, active neurons stay active.

### Derivation of Inactivated Binary Matching (IBM)

IBM uses only the first case from the BM derivation (inactive neurons):

$$\tilde{\gamma}_h[i] = \begin{cases} 0 & \text{if } \gamma_h[i] \leq 0 \wedge h^\ell[i] \leq 0 \\ \gamma_h[i] & \text{otherwise.} \end{cases} \quad (29)$$

**Analysis.** IBM prevents spurious activation of originally inactive neurons. When the optimizer wants to increase an activation ( $\gamma_h[i] \leq 0$ ) but the neuron was originally inactive ( $h^\ell[i] \leq 0$ ), the gradient is clipped. This is a relaxed version of IVM that only constrains inactive neurons.

#### Derivation of Activated Binary Matching (ABM)

ABM uses only the second case from the BM derivation (active neurons):

$$\tilde{\gamma}_h[i] = \begin{cases} 0 & \text{if } \gamma_h[i] > 0 \wedge h^\ell[i] > 0 \\ \gamma_h[i] & \text{otherwise} \end{cases} \quad (30)$$

**Analysis.** ABM prevents spurious deactivation of originally active neurons. When the optimizer wants to decrease an activation ( $\gamma_h[i] > 0$ ) but the neuron was originally active ( $h^\ell[i] > 0$ ), the gradient is clipped. This prevents driving active neurons toward zero.

**Choice of Binary Variants.** The Binary Matching family offers a state-based alternative to Value Matching by constraining only the *activation state* of each neuron (active vs. inactive). In this paper we adopt only the IBM variant, as it provides the minimal constraint necessary to maintain internal consistency without impeding optimization.

Both BM and ABM are unnecessarily restrictive. BM enforces full state preservation, disallowing any increase of inactive neurons or decrease of active neurons. ABM blocks all decreases of active neurons. In practice, most decreases of an active neuron (e.g., 10.0→5.0) do not alter its binary state and thus do not meaningfully affect the computational pathway; nevertheless, BM and ABM would suppress such benign changes, overly constraining the optimization dynamics.

IBM avoids this issue by constraining only the transition that is consistently harmful: the spurious activation of originally inactive neurons. This transition always changes the binary state and corresponds to introducing a new feature direction or pathway. In contrast, the decreases blocked by BM and ABM typically do not cause a state change. Thus, IBM captures the essential asymmetry of binary-state transitions, providing a principled and practical constraint within the Binary Matching family.

### D.3. Summary

The ClipGrad variants provide different levels of constraint on activation modifications:

#### Value Matching Family (L1 Distance):

- **VM (Value Matching):** Strict bidirectional constraint—prevents both suppression and amplification away from original values. Combines AVM and IVM. This variant provides the strongest preservation of internal computation.

- **AVM (Activated Value Matching):** One-sided constraint—prevents suppression below original values, allows amplification. Useful in architectures where decreases of active units are disproportionately harmful.
- **IVM (Inactivated Value Matching):** One-sided constraint—prevents amplification above original values, allows suppression. Suited to settings where spurious amplification is a known issue (e.g., sparse or ReLU-dominated activations).

#### Binary Matching Family (Binary Distance):

- **BM (Binary Matching):** Strict binary state preservation—prevents both activation of inactive neurons and deactivation of active neurons. Combines IBM and ABM.
- **IBM (Inactivated Binary Matching):** One-sided constraint—prevents activation of originally inactive neurons ( $h^\ell[i] \leq 0$ ). Provides maximum optimization flexibility while blocking the most harmful pathway changes.
- **ABM (Activated Binary Matching):** One-sided constraint—prevents deactivation of originally active neurons ( $h^\ell[i] > 0$ ).

**Key Difference.** VM variants preserve the actual activation values using an  $L_1$  distance, while BM variants enforce state preservation by checking only whether the neuron was originally active or inactive.

**Saliency Collapse and Interpretation.** Although the derivation begins with a saliency-weighted internal objective (Eq. 15), the saliency factor cancels with the external gradient in the final expressions, yielding *universal* directional clipping rules that do not discriminate across neurons. This does *not* imply that magnitudes are unimportant. Instead, it reflects the fact that *any* deviation in activation—even on units with low initial saliency—can alter the computational pathway and thus must be regulated uniformly. The derived rules therefore enforce pathway preservation by treating deviations everywhere as potentially meaningful.

### E. Additional Qualitative Comparisons

Figure 8 shows additional attribution visualizations across diverse ImageNet samples on VGG16 and ResNet50. These examples confirm the patterns discussed in the main paper (Sec. 4.5): FEI<sub>NONE</sub> produces noisy attributions, constrained FEI variants generate coherent object-focused maps, and baseline methods like Lift-CAM remain comparatively diffuse.



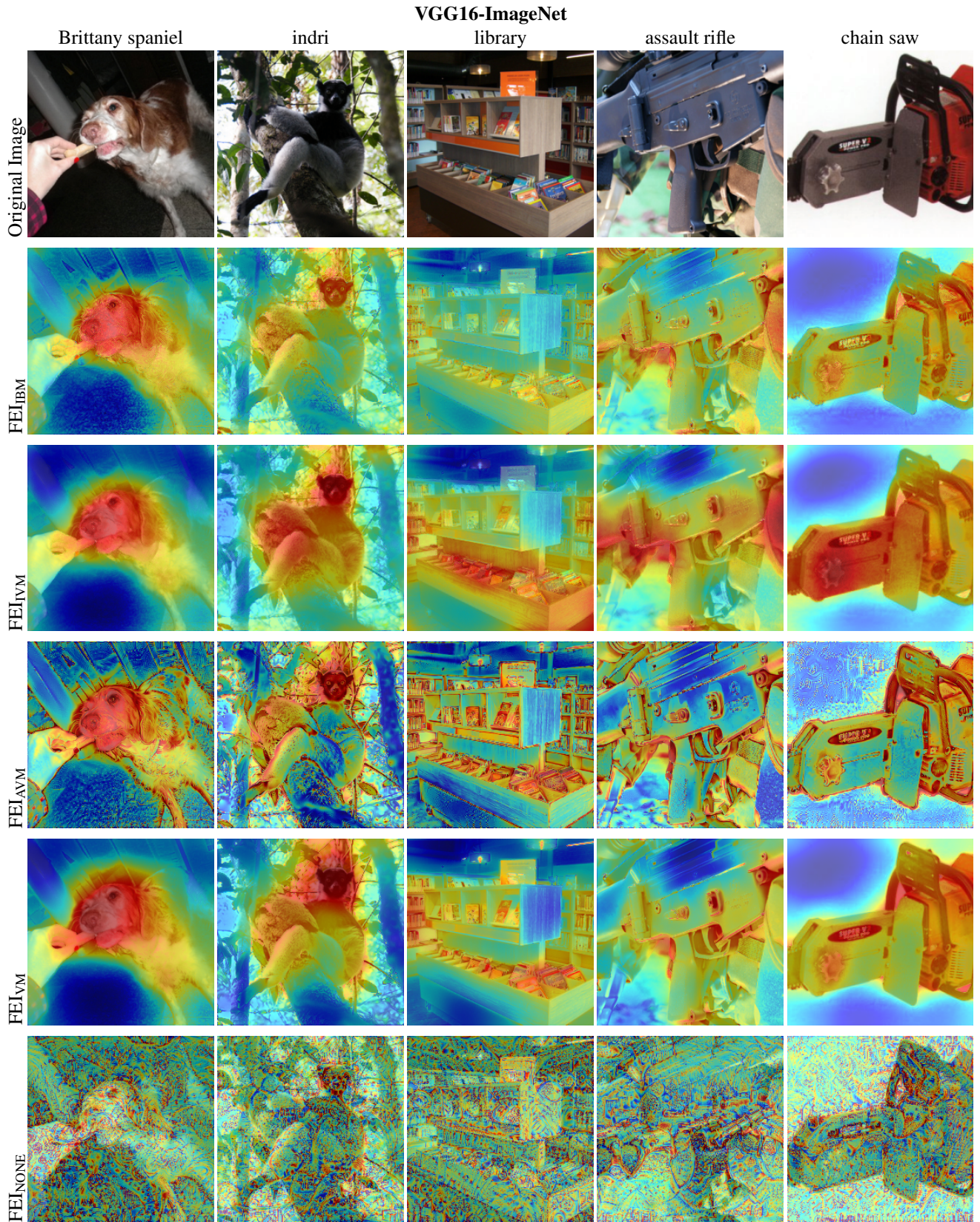


Figure 8. **Additional visual comparison of attribution methods.** Rows show FEI variants, Extremal Perturbation (EP), RISE, IIA, Lift-CAM, and FG-VCE across VGG16-ImageNet and ResNet50-ImageNet. Constrained FEI variants yield more focused, object-aligned explanations compared to baselines, which often highlight background or diffuse regions. (Continued on next page)



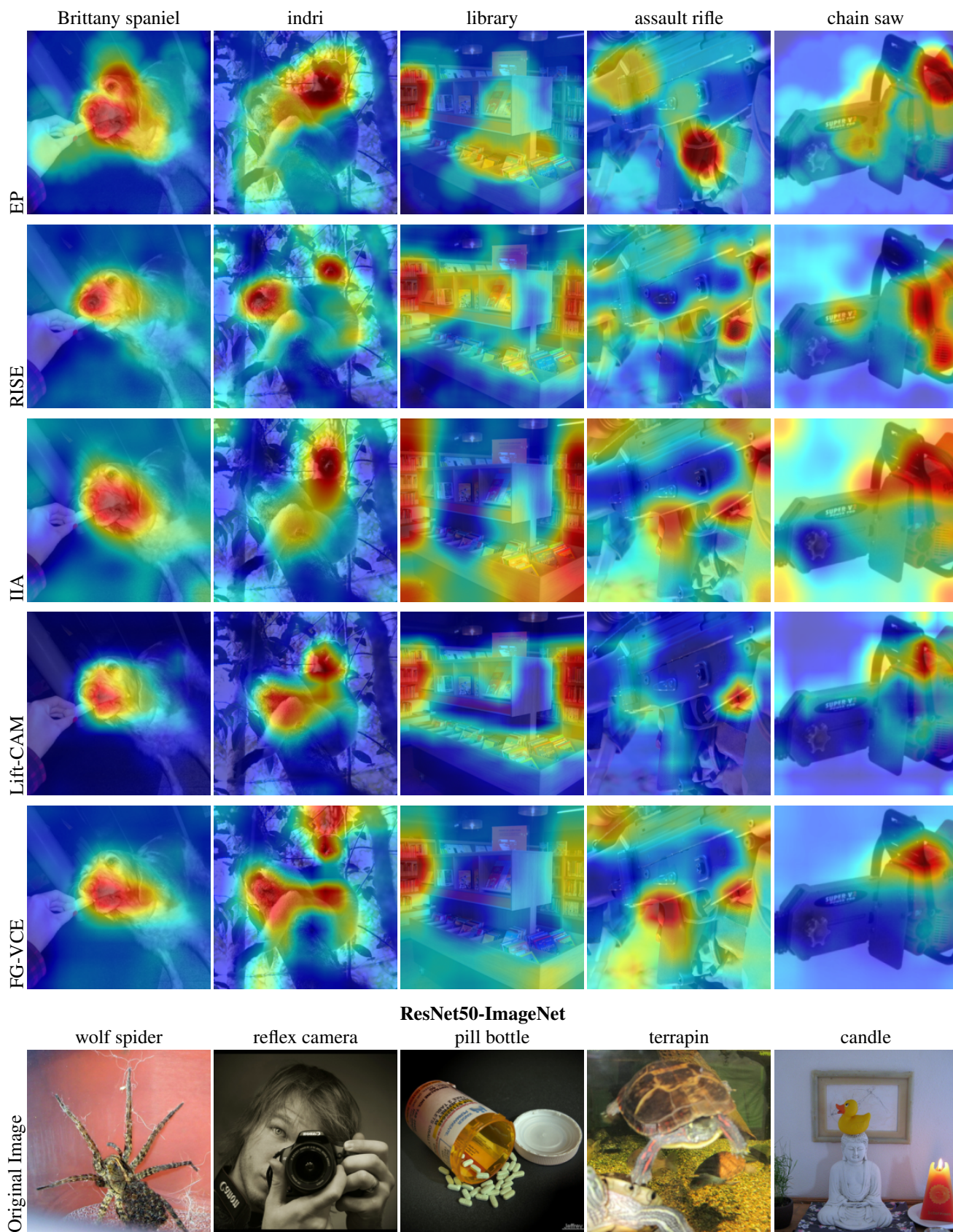


Figure 8. (Continued) Additional visual comparison of attribution methods.



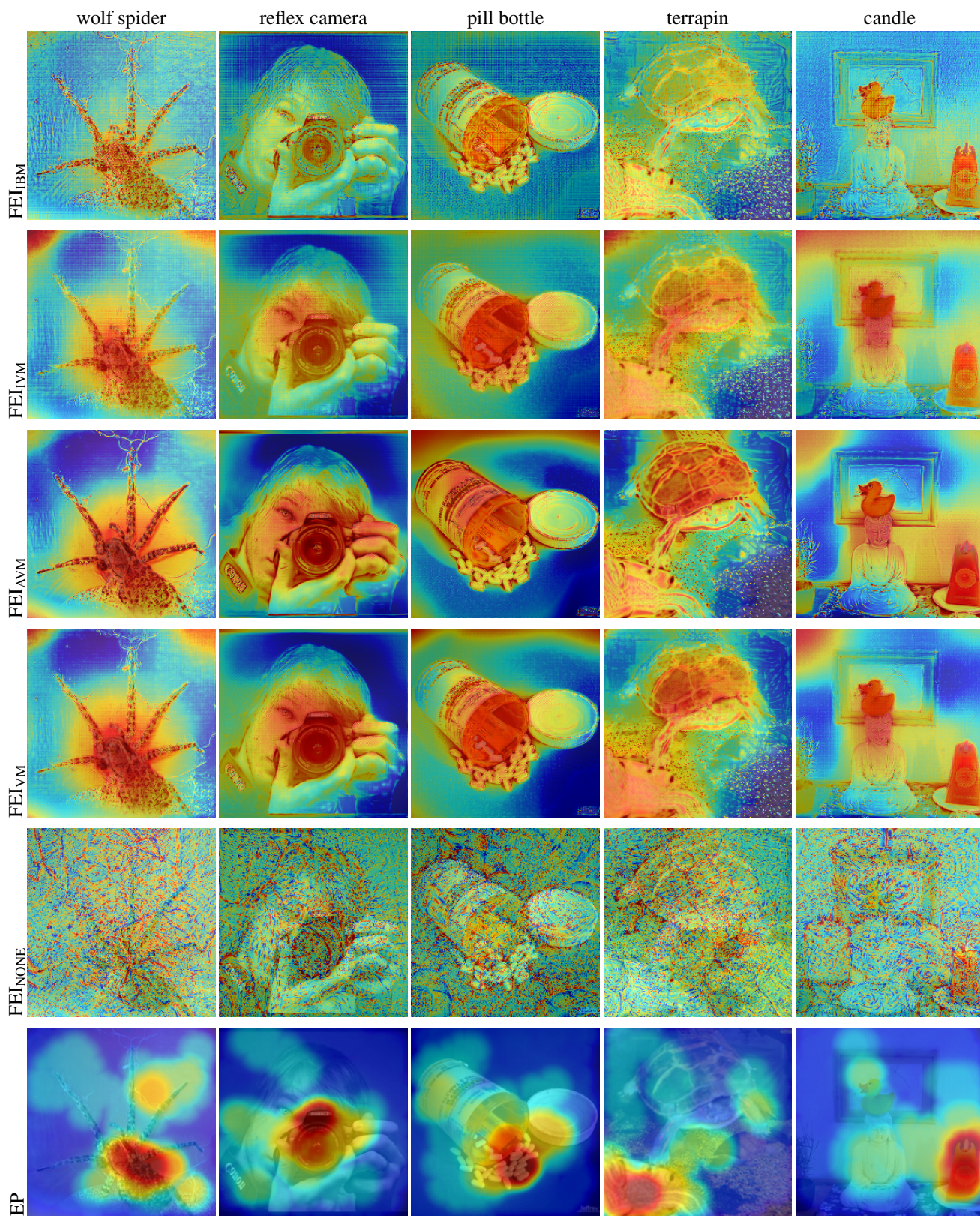


Figure 8. (Continued) Additional visual comparison of attribution methods.



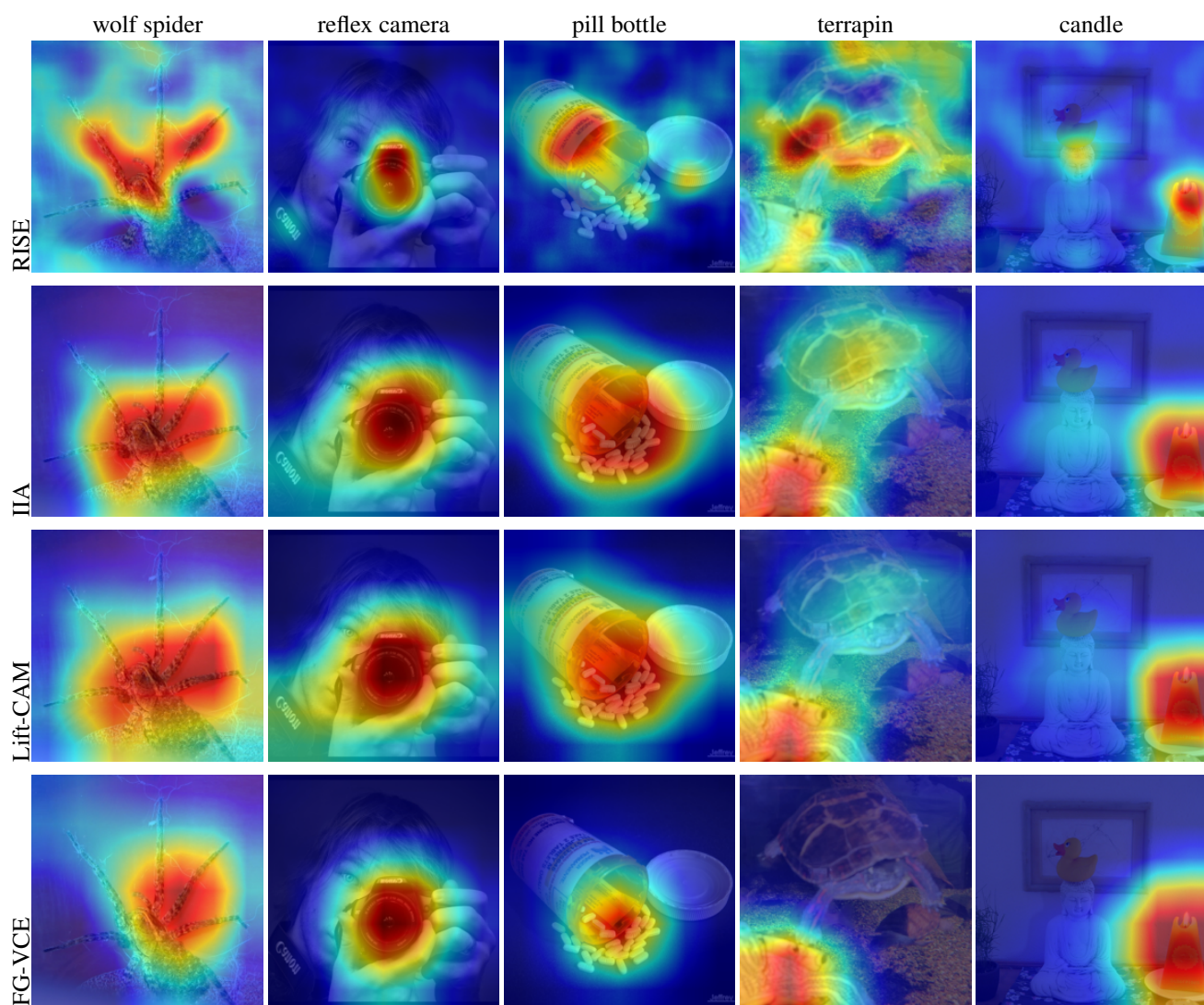


Figure 8. (Continued) **Additional visual comparison of attribution methods.**